Time-dependent decrease in fault strength in the 2011–2016 Ibaraki–Fukushima earthquake sequence

Sam Wimpenny [1,2] Natalie Forrest [1,2] and Alex Copley[1]

[1]*COMET, Bullard Laboratories, Department of Earth Sciences, University of Cambridge, Cambridge CB2 3EQ, UK. E-mail:* earswi@leeds.ac.uk
[2]*COMET, School of Earth and Environment, University of Leeds, Woodhouse, Leeds LS2 9JT, UK*

SUMMARY

Two near-identical M_w 5.8 earthquakes in 2011 and 2016 ruptured the Mochiyama Fault in the Ibaraki–Fukushima region of Japan. The unusually short repeat time between the two earthquakes provides a rare opportunity to estimate the evolution of stress on a fault through an earthquake cycle, as the stress drop in the first earthquake provides a reference value from which we can infer variations through time in the stresses required to cause earthquake rupture. By combining observations of crustal deformation from GPS, InSAR and seismology with numerical models of stress transfer due to coseismic deformation and post-seismic relaxation, we demonstrate that the rupture area on the Mochiyama Fault could only have been reloaded by up to 50–80 per cent of the 2011 earthquake stress drop (3–10 MPa) between that event and the subsequent 2016 earthquake. Most of this reloading was caused by afterslip around the rupture area driven by stress changes from the 2011 Mochiyama and Tohoku-oki earthquakes. We therefore infer that the Mochiyama Fault became weaker in the intervening 6 yr, with at least a 1–5 MPa drop in the shear stresses needed to break the fault in earthquakes. The mechanism(s) that led to this weakening are unclear, but were associated with extensive aftershock seismicity that released a cumulative moment similar to the 2011 main shock. Temporal changes in fault strength may therefore play a role in modulating the timing of moderate-magnitude earthquakes.

Key words: Earthquake dynamics; Dynamics and mechanics of faulting; Rheology and friction of fault zones.

1 INTRODUCTION

Earthquakes are generated by the accumulation of elastic strain around a fault zone, and its eventual release when the shear stress resolved on the fault exceeds the frictional resistance to slip (Reid 1910). However, a deterministic application of this 'elastic rebound theory' to estimate the timing of large earthquakes has proven difficult (e.g. Roeloffs & Langbein 1994), because the absolute state of stress on faults cannot be easily measured, the evolution of stress and strain between earthquakes is typically too long to be inferred from geodetic measurements of deformation, and the strength of active faults, and how fault strength varies in space, remain controversial topics. In addition, where the timing of multiple earthquakes on a particular fault patch are well documented, they sometimes show non-periodic repeat times (Murray & Segall 2002; Sieh *et al.* 2008; Fukushima *et al.* 2018). This observation suggests that the rate of fault loading, or alternatively the fault strength, may also vary with time to produce 'non-characteristic' earthquakes on some faults (Kagan *et al.* 2012).

Two near-identical M_w 5.8 normal-faulting earthquakes near Mochiyama in the Ibaraki–Fukushima region of Japan on the 19th

March 2011 and 28th December 2016 provide a rare opportunity to determine the evolution of stress on a fault through a whole earthquake cycle (Fig. 1). A previous study of the slip distributions in the Mochiyama earthquakes demonstrated that the two events ruptured the same area of the NNW–SSE striking Mochiyama Fault between the surface and 7 km depth (Figs 1b and c; Fukushima *et al.* 2018; Komura *et al.* 2019). Therefore the same patch of fault reached its failure stress twice in the space of ∼6 years. Between the two earthquakes, Japan's GEONET GPS network captured significant extensional strain localized across the Mochiyama Fault. Fukushima *et al.* (2018) argued that this deformation may reflect rapid reloading of the fault through extensive post-seismic afterslip caused by the coseismic stress changes from the 2011 Mochiyama earthquake and the post-seismic stress changes following the 2011 Tohoku-oki earthquake. However, they found that a model in which afterslip was driven by these stress changes could only account for a small fraction of the observed interevent strain, and could only reload the Mochiyama Fault by less than 10–20 per cent of the coseismic stress drop.

The Mochiyama earthquakes formed part of a sequence of seismicity in the Ibaraki–Fukushima region that began after the
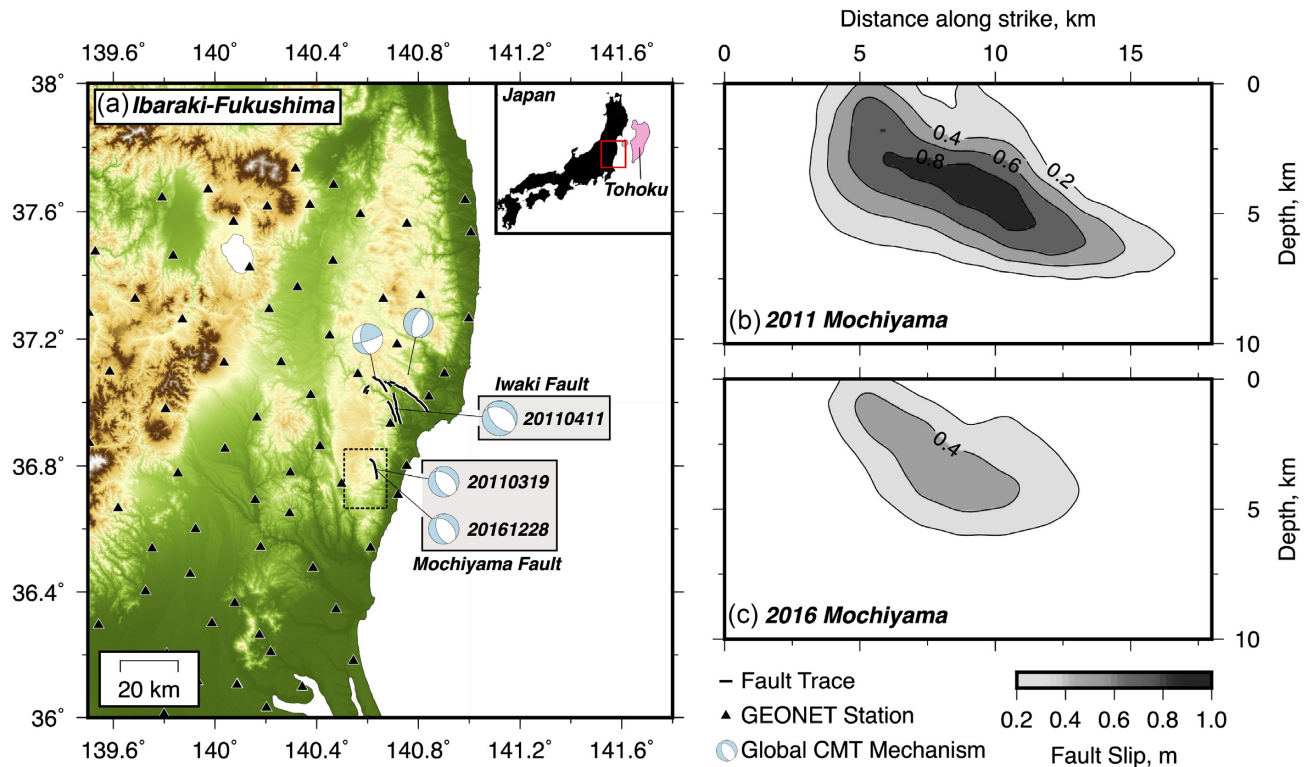
Figure 1. Overview of the Ibaraki–Fukushima earthquake sequence. (a) Map of the study region showing the locations and Global CMT mechanisms of the Mochiyama and Iwaki earthquake sequences (Ekström *et al.* 2012). GEONET GPS stations are shown as black triangles and the surface rupture traces from Toda & Tsutsumi (2013) and Komura *et al.* (2019) as black lines. The dashed black box is the area covered by coseismic and post-seismic SAR measurements shown in Fig. 4. The inset map shows the location of the study region relative to the 10 m coseismic slip contour in the M_w 9.1 11th March 2011 Tohoku-oki earthquake taken from Hayes (2017). Panels (b) and (c) show the slip distributions in the 2011 and 2016 Mochiyama earthquakes determined by Fukushima *et al.* (2018). The slip distribution in (b) was derived using two ALOS-1 interferograms spanning the dates 2011/02/02–2011/03/20 for the ascending track and 2010/11/20–2011/04/07 for the descending track. The slip distribution in (c) was derived using three ALOS-2 frames spanning 2016/11/15–2017/02/21 and 2016/11/01–2017/02/07 from the ascending track and 2016/11/17–2016/12/29 from the descending track, plus static GPS displacements from the GEONET network.

11th March 2011 M_w 9.1 Tohoku-oki earthquake, and which included three other moderate-magnitude earthquakes within 20 km of Mochiyama in March and April 2011 (Imanishi *et al.* 2012; Fukushima *et al.* 2013; Fig. 1a). These earthquakes generated coseismic displacements that will have also changed the stress state on the Mochiyama Fault (King *et al.* 1994). The stress changes will have been at least partially relaxed through afterslip and aftershocks within the seismogenic crust, and distributed viscous flow or localized viscous shear within the aseismic lower crust and upper mantle (Freed 2005), causing time-dependent loading of the Mochiyama Fault between 2011 and 2016. As all of these stress changes were not included in the original calculations of Fukushima *et al.* (2018), and because their calculations could not account for the observed deformation, it remains unclear whether the Mochiyama Fault was fully reloaded back to its former failure stress, or whether the fault became weaker and ruptured at a lower failure stress in 2016. Addressing this question is clearly critical to developing our understanding of the controls on the strength of active faults and for building deterministic models of the earthquake cycle and seismic hazard.

In this study, we build upon the work of Fukushima *et al.* (2018) and determine the coseismic and time-dependent stress changes on the Mochiyama Fault through the Ibaraki–Fukushima earthquake sequence. We then use these stress change calculations to investigate potential temporal changes in the stresses required to break the fault in earthquakes. We begin by making new geodetic and seismological

observations of the earthquake sequence in Section 2 to place constraints on the mechanisms that loaded the Mochiyama Fault. We then develop a series of forward models in Section 3 to determine by how much each different mechanism could have reloaded the Mochiyama Fault within the limits of the observed deformation. These models extend the previous work of Fukushima *et al.* (2018) by: (1) gaining more general insight into the ways post-seismic relaxation reloads fault zones and (2) by performing a wide range of models that allow us to assess how variations in the rheology of the Earth might translate into estimates of fault reloading and surface strain. From our modelling we find that the Mochiyama Fault could only have been reloaded by up to 50–80 per cent of the coseismic stress drop of the 2011 earthquake by the time the 2016 earthquake reruptured the fault. In Section 4, we discuss the implications of this result for the time-dependent strength of active faults.

2 OBSERVATIONS OF THE IBARAKI–FUKUSHIMA EARTHQUAKE SEQUENCE

2.1 Long-period body-waveform modelling

We first determined the focal mechanisms, centroid depths, source–time functions and moment releases of the 2011 and 2016 Mochiyama earthquakes by inverting their long-period teleseismic
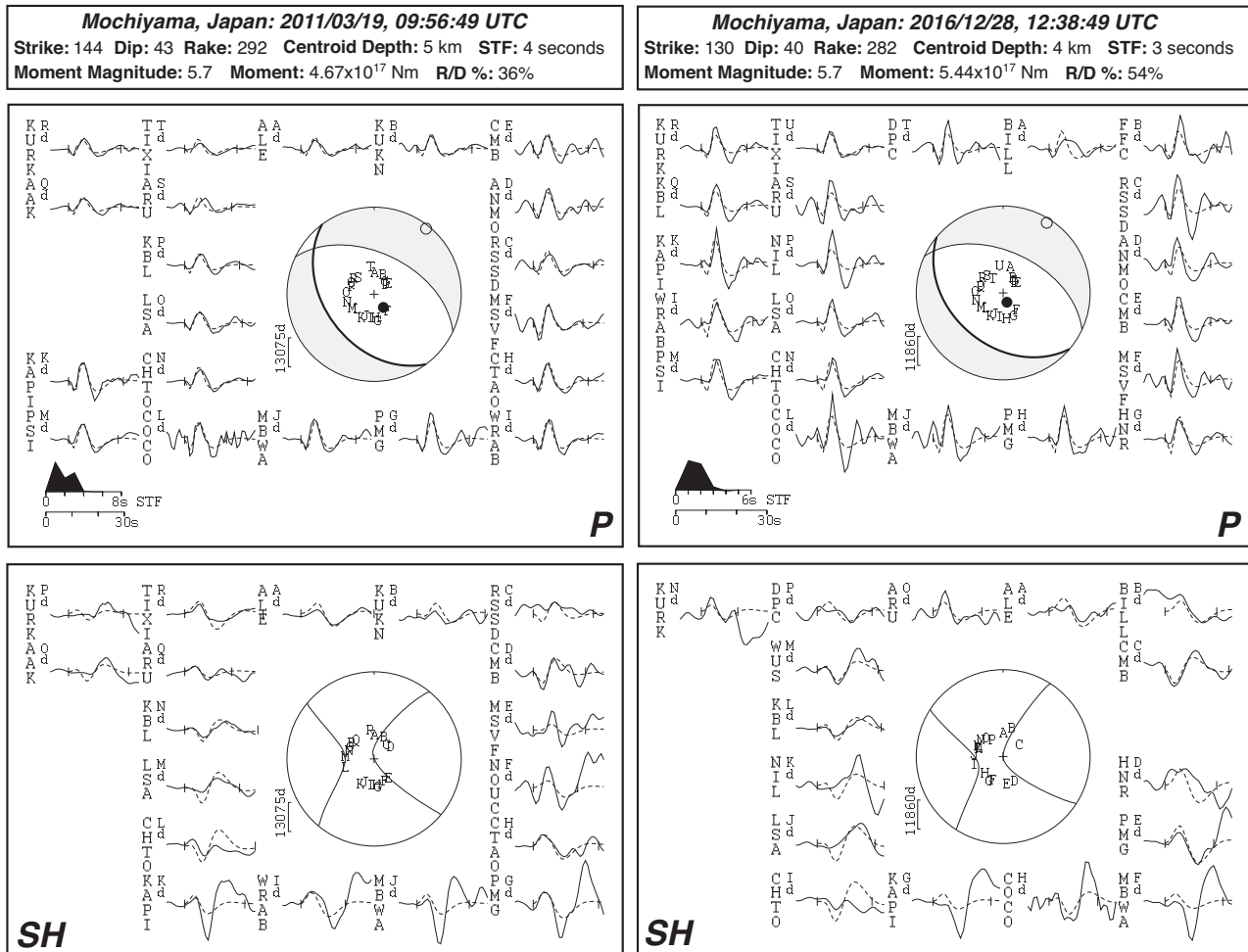
Figure 2. Minimum-misfit body-waveform models for the 2011 and 2016 Mochiyama earthquakes. The minimum-misfit parameters for each model are shown in the top panels, where STF is the source-time function and R/D per cent is the ratio of the residual variance to the data variance expressed as a percentage. The middle panel shows the fit between the modelled (dashed) and observed (solid) waveforms for the *P* waves. Each seismogram has to its left the three/four-letter station code, and a capital letter that corresponds to the letters plotted on the focal sphere. The source–time function and timescale for the plotted waveforms is shown in the bottom left. The *SH* waveforms are shown in the bottom panel using the same format.

P and *SH* seismograms using synthetic waveforms of the *P*, *S*, *pP*, *sP* and *sS* phases, modelled assuming a finite-duration rupture at a point source (Nabalek 1984; Zwick *et al.* 1994). This method has been widely used and described because of its sensitivity to the mechanisms and centroid depths of shallow moderate-magnitude earthquakes (e.g. McCaffrey & Abers 1988; Taymaz *et al.* 1990). Therefore further details of the modelling are provided in Text S1.

The long-period waveforms of both earthquakes can be well matched at most stations using this method (Fig. 2). The minimum-misfit solution for the 2011 earthquake has a seismic moment of 4.7×10^{17} Nm (M_w 5.7), a source–time function length of 3 s, a strike/dip/rake of the southwest dipping nodal plane of 295/51/–109 and a 5 km centroid depth (Fig. 2a). The moment is similar to estimates from the USGS W-Phase (4.3×10^{17} Nm), USGS body wave (4.5×10^{17} Nm) and Global Centroid Moment Tensor (6.9×10^{17} Nm) methods, but is only 40 per cent of that derived from the InSAR-based coseismic slip inversion of Fukushima *et al.* (2018) (1.2×10^{18} Nm) when calculated using the same shear modulus. The 2016 earthquake has a near-identical minimum-misfit solution, with a moment release of 5.4×10^{17} Nm, a source-time function length of 4 seconds, a strike/dip/rake of 295/51/–100 and a centroid depth of 4 km (Fig. 2b). The seismic moment estimate is identical

to the geodetic moment derived by Fukushima *et al.* (2018) (5.4×10^{17} Nm) when using the same shear modulus. For both earthquakes, the centroid depth and moment release trade-off against one another, as at shallower depths the depth-phases destructively interfere with the direct phase meaning a larger moment is needed to account for waveforms of a given amplitude (Christensen & Ruff 1985; Taymaz *et al.* 1990). By varying the centroid depth during the inversions between 3 and 7 km, which is the InSAR-derived range of peak coseismic slip (Figs 1b and c), the minimum-misfit moment release in both earthquakes ranges from 3 to 6×10^{17} Nm.

Given that the amplitude of post-seismic deformation scales with the coseismic moment (Churchill *et al.* 2022), our new estimate of the coseismic moment of the 2011 Mochiyama earthquake will have important implications for the predicted post-seismic deformation. The likely explanation for the difference between the seismic and geodetic moment estimates is that the interferograms used by Fukushima *et al.* (2018) to invert for the pattern of slip in the 19th March 2011 Mochiyama earthquake (which span the dates 2011/02/02–2011/03/20 for the ascending track and 2010/11/20–2011/04/07 for the descending track) contain some surface deformation that was not caused by coseismic slip. One possible source of deformation was a series of shallow M_w 4–5 earthquakes within the

fault's hangingwall that were triggered by the 11th March Tohoku-oki earthquake (Fukushima *et al.* 2018). These small earthquakes align on a northeast dipping conjugate plane seen in the relocated aftershock seismicity (Fig. S1). By mapping the surface deformation from these small, shallow earthquakes into deep coseismic slip on the Mochiyama Fault, Fukushima *et al.* (2018) could have overestimated the coseismic moment release in the 19th March Mochiyama earthquake. The interferograms used to invert for the pattern of coseismic slip may also contain some surface deformation caused by early post-seismic slip, which would also lead to an overestimate of the coseismic moment release (e.g. Twardzik *et al.* 2019). In the following sections, we show that the GPS and microseismicity measurements support the conclusion that the moment release in 19th March 2011 earthquake derived from the slip inversion of Fukushima *et al.* (2018) is an overestimate.

2.2 GPS

We collected the F3 solutions of daily position time-series for each GPS station in Japan's GEONET network and used a trajectory-modelling approach (e.g. Bedford *et al.* 2020) to fit the observed displacements with an arbitrary combination of steps, linear ramps, logarithmic terms and sinusoids using a non-linear least-squares routine implemented in SciPy (Virtanen *et al.* 2020). After the first attempt to fit the time-series, we stacked the residuals between the trajectory models and the observed time-series at every station to determine the common-mode error and removed it from the observed time-series (Wdowinski *et al.* 1997). We then fit these corrected time-series with an updated trajectory model, yielding a smooth approximation of the displacement through time at each GPS station. Final residuals between the trajectory models and the corrected displacement time-series, which we interpret to represent random noise that is not caused by tectonic deformation, were consistently Gaussian with a standard deviation of 2–3 mm and a mean of 0 mm.

The vertical and horizontal displacements are dominated by an eastward translation and uplift caused by post-seismic relaxation after the Tohoku-oki earthquake. Therefore, to determine the evolution of deformation in the study region, we calculated the 2-D incremental strain tensor over different epochs using the triangular interpolation method of Bourne *et al.* (1998) and the trajectory models of the displacements. This method does not enforce any spatial smoothing on the strain field, therefore can identify strain signals on the length scale of the station spacing. The noise levels in the displacement measurements translate into an uncertainty of ∼0.2–0.3 microstrain in the strain measurements, given the typical station spacing in the network of 15–20 km. The vertical displacements do not contain any clear signals related to the Ibaraki–Fukushima earthquake sequence beyond those associated with the coseismic displacements in the Tohoku-oki and Iwaki earthquakes, and therefore we do not consider them further here.

On the 19th March 2011 the first earthquake to rupture the Mochiyama Fault generated predominantly 1.6 microstrain of NE–SW to ENE–WSW extension in the triangles spanning the fault zone, and predominantly 1 microstrain contraction in triangles to the southwest of the fault (Fig. 3a). A forward calculation of the coseismic strain predicted by the slip model of Fukushima *et al.* (2018) can match the pattern of the observed strain, but significantly overpredicts the strain amplitude (Fig. S2a). Therefore we performed a grid search of coseismic slip models in which we applied a scaling factor to the slip distribution, and searched for the models that best fit the coseismic strain field. We found that models with a moment release of $5–6 \times 10^{17}$ Nm best fit the strain observations

(Fig. S2b), which is consistent with the moment release determined by the long-period body-waveform modelling presented in Section 2.1 ($3–6 \times 10^{17}$ Nm).

In the month that followed the 2011 Mochiyama earthquake, the GPS network recorded a further 1.2 microstrain of NE–SW post-seismic extension across the Mochiyama Fault (Fig. 3b), and 4–5 microstrain of NW–SE extension generated by a M_w 5.9 normal-faulting earthquake on the 23rd March 2011 (Fukushima *et al.* 2013; Fig. 3b). Outside of the epicentral region of these earthquakes, the Ibaraki–Fukushima area was being stretched ∼E–W by 0.2–0.4 microstrain as a result of ongoing post-seismic relaxation following the Tohoku-oki earthquake (Hu *et al.* 2016).

The largest earthquake within the sequence occurred on the 11th April 2011: a M_w 6.6 earthquake that simultaneously ruptured two NW–SE trending normal faults 20 km north of Mochiyama near the city of Iwaki (known herein as the 'Iwaki Faults'). The Iwaki earthquake was followed a day later by a M_w 5.9 strike-slip aftershock. These two earthquakes generated 20–25 microstrain of extension across the Iwaki Faults and 0.7 microstrain of extension across the Mochiyama Fault (Fig. 3c).

Between May 2011 and December 2016 there were no more $M_w > 5$ earthquakes in the study area. GPS stations that span the Mochiyama Fault measured 2–3 microstrain of ENE–WSW extension (Fig. 3d) that followed a logarithmic decay in time. Elsewhere, almost all of the study region experienced ∼2 microstrain of shear with the maximum principal strain axis being oriented ∼E–W to NW–SE, and the minimum principal strain axis oriented ∼N–S to NE–SW. This regional pattern of shear strain represents the deformation of the Japanese mainland caused by post-seismic relaxation following the Tohoku-oki earthquake (e.g. Hu *et al.* 2016; Becker *et al.* 2018).

The cumulative strain between the 2011 and 2016 Mochiyama earthquakes (the 'interevent period') represents the horizontal surface strain associated with reloading of the Mochiyama Fault (Fig. 3e). The strain across the fault consisted of 3.8–4.3 microstrain of extension—0.7 microstrain of which can be attributed to the static deformation caused by the Iwaki earthquakes. Any model of the reloading of the Mochiyama Fault must account for the remaining 3.1–3.6 microstrain of observed across-fault stretching through predominantly aseismic deformation mechanisms. Within the triangles to the southwest of the fault that span the fault's hangingwall, the strain field records incremental contraction. Notably, the orientation of the principal strain axes in triangles that span the Mochiyama Fault, and triangles in the immediate fault hangingwall, are subparallel to the principle axes of the coseismic strain field in the 2011 Mochiyama earthquake (compare Fig. 3a with Fig. 3e). Therefore, the sense of aseismic strain around the Mochiyama Fault over the interevent period can be accounted for by post-seismic aseismic slip ('afterslip') on the main shock fault plane within a similar depth-range to coseismic slip.

On the 28th December 2016 the second earthquake re-ruptured the Mochiyama Fault and generated 2 microstrain of ENE–WSW to NE–SW extension across the fault zone with a similar pattern to the 2011 earthquake (Fig. 3f). The across-fault extension in 2016 was slightly larger than in 2011, which supports the conclusion from the long-period body-waveform modelling that the 2016 earthquake had a slightly larger moment release than in 2011. Over the post-seismic period between December 2016 and December 2017, the GPS network captured ∼0.3 microstrain of logarithmically decaying post-seismic extension across the Mochiyama Fault (Fig. S3), which was 10 times smaller than the strain recorded in the year after the 2011 earthquake. Despite the stark difference in the amplitude of the
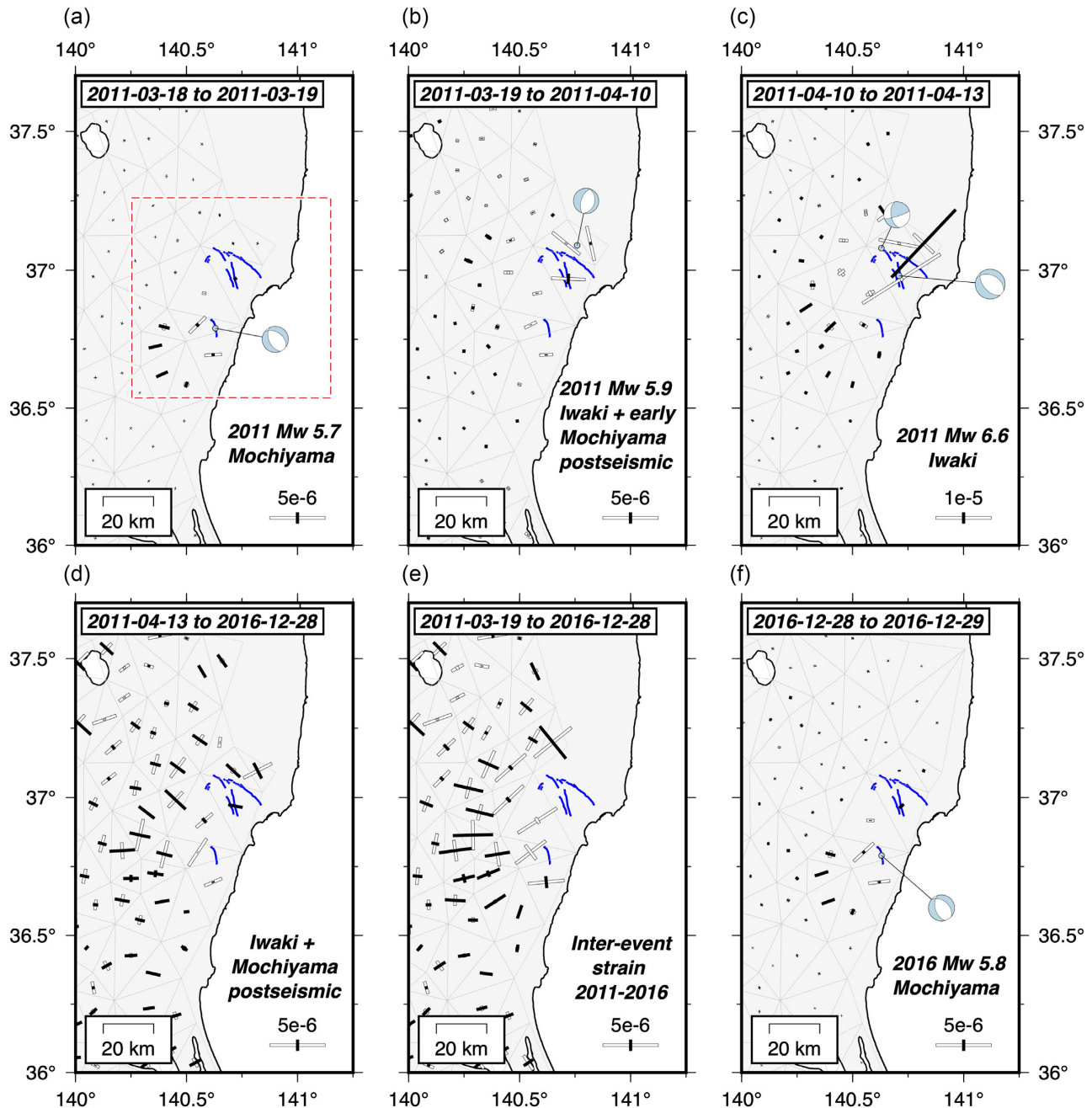
Figure 3. Incremental strain through the 2011–2016 Ibaraki–Fukushima earthquake sequence. White bars represent principal axes of extensional strain, whilst black bars are principal axes of contractional strain. Note the difference in bar scaling between certain epochs. Blue lines are the surface traces of the Mochiyama and Iwaki Faults from Fukushima *et al.* (2013) and Komura *et al.* (2019), and the red dashed box in (a) is the map area shown in Figs 5 and 8. The GPS triangles spanning the Iwaki Fault are removed from (e) to highlight the interevent strain across the Mochiyama Fault.

post-seismic strain measured after the 2011 and 2016 Mochiyama earthquakes, the relaxation time of the strain transients were near-identical (Fig. S4).

In the 6 years prior to the Mochiyama and Tohoku-oki earthquakes (2005–2011), the strain field across the Mochiyama Fault consisted of 1–2 microstrain of simple shear with the minimum principle axis of strain oriented ∼N–S to NW–SE (Fig. S3a). This interseismic strain is not consistent with signals produced by localized shear downdip of the rupture area, which could load the Mochiyama Fault towards failure (see further discussion in Section 3.2). On the 11th March 2011, coseismic slip in the Tohoku-oki earthquake

led to E–W stretching of the region around the Mochiyama Fault by 10 microstrain (Fig. S3b), and was followed by a further 0.4 microstrain of ∼E–W stretching between the 11th and 18th March (Fig. S3c), which will have loaded the Mochiyama Fault towards failure (Ozawa *et al.* 2011).

2.3 Radar geodesy

Fukushima *et al.* (2018) and Komura *et al.* (2019) previously formed ALOS interferograms of the coseismic deformation in the 2011 and 2016 Mochiyama earthquakes (Figs 4a and c). The two earthquakes
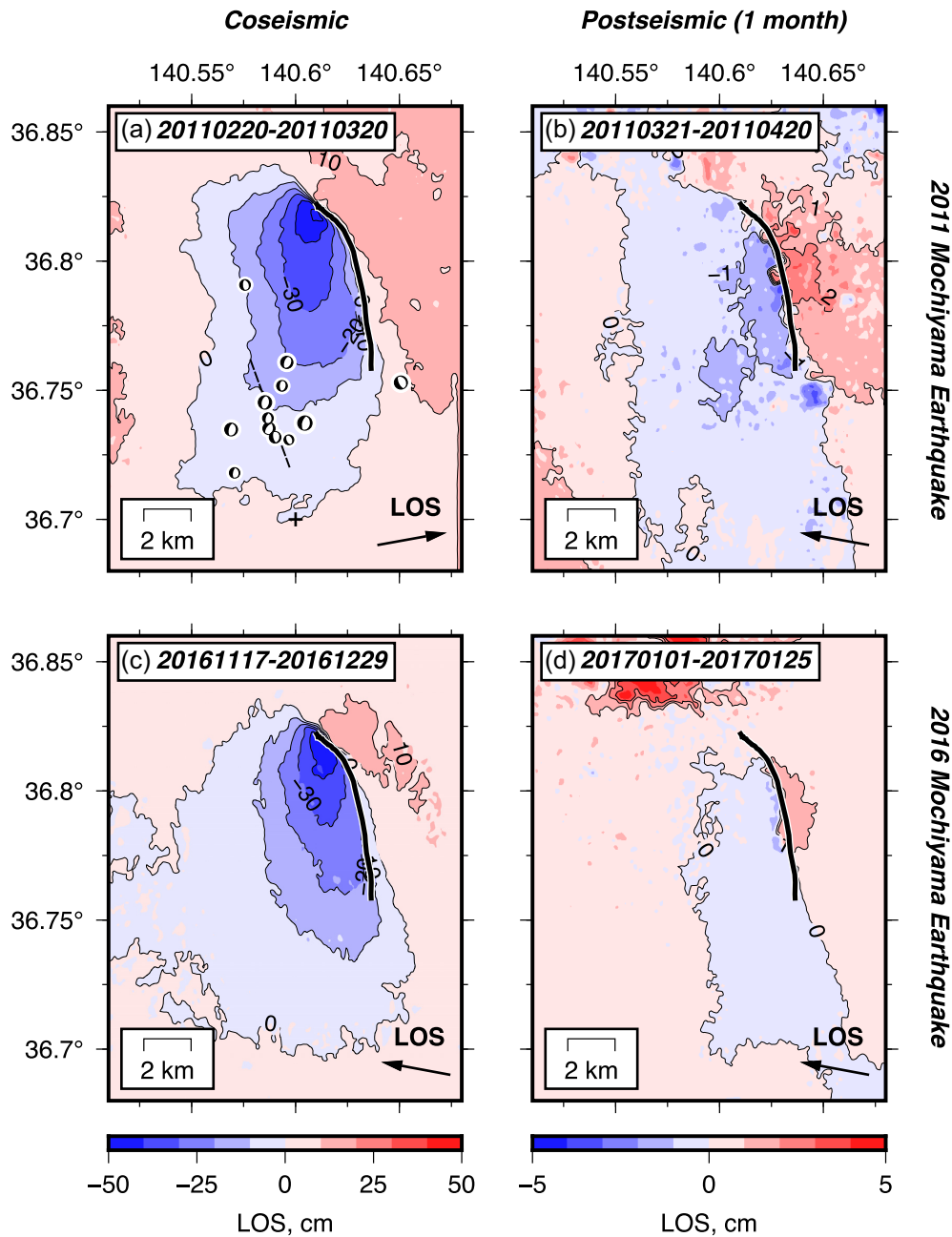
Figure 4. Coseismic and early post-seismic interferograms from the 2011 and 2016 earthquakes on the Mochiyama Fault. The surface trace of the fault is shown by the thick black line and the date of the primary and secondary acquisition is shown in the top left in yyymmdd format. Line-of-sight vectors are shown in the bottom right. (a) ALOS-1 ascending track coseismic interferogram showing the LOS displacement in the 19th March 2011 Mochiyama earthquake from Komura *et al.* (2019). The interferogram contains 1 day of post-seismic deformation. Focal mechanisms are M_w 4 and 5 foreshocks that occurred between the 11th March 2011 and 18th March 2011 from the NIED catalogue. The black-dashed line indicates the strike of the conjugate normal fault seen in the relocated microseismicity (Fig. S1). (b) Envisat descending track interferogram of the first month of post-seismic relaxation after the 2011 earthquake covering the period of 2–32 days after the main shock. (c) ALOS-2 descending track coseismic interferogram covering the 28th December 2016 Mochiyama earthquake from Komura *et al.* (2019). The interferogram contains 1 day of post-seismic deformation. (d) Sentinel-1 descending track interferogram of the first month of post-seismic relaxation after the 2016 earthquake covering the period of 4–28 days after the main shock.

generated near-identical patterns of coseismic surface deformation, suggesting the slip distributions overlapped significantly at depth. The interferograms record peak line-of-sight (LOS) displacements of 40–60 cm and a sharp offset in LOS across the north-western fault tip. The LOS displacements decrease in amplitude, and become smoother, towards the southeastern fault tip. These features of the data suggest that peak slip in both earthquakes overlapped on the

northwestern portion of the fault, and that slip became buried and decreased towards the southeast (Fukushima *et al.* 2018; see Figs 1b and c). Given that both earthquakes had similar seismic moment release, and similar rupture areas, then it is likely that they had similar stress drops.

For the 2011 Mochiyama earthquake, the coseismic interferogram in Fig. 4(a) shows an increase in the wavelength of the

hangingwall subsidence towards the southern edge of the fault. This is the same area that experienced shallow M_w 4 and 5 normal-faulting foreshocks between the 11th March and 19th March 2011, which may have contributed to the surface deformation measured by InSAR (Fukushima *et al.* 2018).

To measure the post-seismic deformation around the Mochiyama Fault we formed Envisat ASAR interferograms from the descending track 347, which start from the 21st March 2011 (2 days after the main shock) and cover the first 7 months after the 2011 Mochiyama earthquake. Envisat stopped transmitting data at the end of 2011, therefore we could only measure the early post-seismic deformation. The SAR data was processed using ISCE and a 30 m SRTM Digital Elevation Model (Farr *et al.* 2007) to remove the topographic contribution to phase. The interferograms were unwrapped using the statistical-cost network flow algorithm SNAPHU (Zebker & Lu 1998). We also applied a Gaussian filter to the interferograms with a half-width of 0.5 km and removed a planar ramp.

Much of the region around the Mochiyama Fault is covered in thick vegetation, and therefore the C-band data suffered from decorrelation. Nevertheless, in the first 2–32 days following the 2011 Mochiyama earthquake one post-seismic interferogram with good coherence could be formed (Fig. 4b). A step of 4–5 cm in LOS displacement can be seen across the surface trace of the Mochiyama Fault. The sharp offset in LOS displacement is mainly concentrated to the southeast of the area of peak coseismic LOS displacement, which is a common observation following normal-faulting earthquakes and reflects afterslip on the shallow portion of the main shock rupture plane (e.g. Cheloni *et al.* 2010). At distances of ∼5–10 km from the fault, the relative LOS displacements across the fault are <1–2 cm, which limits the amount of deep afterslip or ductile flow that occurred in the first month after the 2011 earthquake.

We also formed interferograms using Sentinel-1 SAR data covering the first 4–28 days of post-seismic deformation following the 2016 Mochiyama earthquake, using the same processing work flow. The Sentinel-1 measurements reveal a sharp ∼2 cm step in LOS displacement across the fault, and <1 cm of relative LOS displacement at distances >5 km from the surface trace of the fault (Fig. 4d). The patterns of near-field post-seismic deformation are similar in the first month following the two earthquakes. However, the 2016 earthquake was followed by less shallow afterslip.

2.4 Aftershock seismicity

The locations, magnitudes and focal mechanisms of small earthquakes provide additional constraints on the deformation in the region of the Mochiyama Fault. We use the hypocentral locations determined by Uchide & Imanishi (2018), which are based on the Japan Meteorological Agency (JMA) unified catalogue that have been relatively relocated using the double-difference method (Waldhauser & Ellsworth 2000). Focal mechanisms derived by the National Research Institute for Earth Science and Disaster Resilience (NIED) provide additional constraints on the sources of microseismicity.

The 2011 Mochiyama earthquake was followed by a large number of normal-faulting aftershocks (Fig. 5a) concentrated almost entirely between 5 and 10 km depth (Fig. S5). The aftershocks were clustered around the margins and base of the rupture area, and delineate a planar structure dipping 40–60° towards the southwest (Kato *et al.* 2011). Aftershocks recorded in the 2 yr following the 2016 Mochiyama earthquake also had mostly normal-faulting mechanisms (Fig. 5b), and were concentrated beneath the downdip edge

of the rupture area (Fig. S5). The similarity between the aftershock and the main shock mechanisms, and the alignment of the microseismicity with the along-strike and downdip projection of the main shocks, imply that the aftershocks reflect slip on the Mochiyama Fault around the margins of the coseismic rupture.

Although the mechanisms and magnitudes of the 2011 and 2016 Mochiyama earthquakes were similar, the moment release in their aftershock sequences was significantly different (Figs 5c–f). The first six months after the 2011 earthquake was characterized by aftershock moment release that followed a logarithmic decay, mirroring the across-fault strain measured by the GPS network (Figs 5c and e). Most unusually, though, was that the cumulative moment release from aftershocks in the region directly around the Mochiyama Fault in the period May 2011 to December 2016 was $6 \pm 2 \times 10^{17}$ Nm, which is similar in magnitude to the 2011 main shock moment release ($3–6 \times 10^{17}$ Nm). Aftershock sequences typically only account for between 1 and 20 per cent of the main shock moment (Zakharova *et al.* 2013), suggesting the seismicity that followed the 2011 Mochiyama earthquake was unusually energetic. The 2016 earthquake was followed by little across-fault extensional strain (Fig. 5d) and a less energetic aftershock sequence that released only $1.8 \pm 0.8 \times 10^{17}$ Nm within 2 yr of the main shock (Fig. 5f), which equates to a third of the main shock moment release.

2.5 Summary of the key observations

The InSAR and body-waveform modelling show that the 2011 and 2016 earthquakes ruptured the same area of the Mochiyama Fault in two earthquakes with near-identical magnitudes. Over the interevent period between these two earthquakes, the GPS network captured 3.1–3.6 microstrain of across-fault extension that could not be attributed to any moderate-magnitude seismicity. In GPS triangles that span the fault hangingwall, the sense of strain over the interevent period was contractional. Post-seismic InSAR observations demonstrated that some of this strain derived from at least ∼4–5 cm of shallow afterslip above the coseismic rupture on the Mochiyama Fault. Extensive aftershocks around the margins of the coseismic rupture suggest that fault slip was also prevalent at depth, extending down to at least 10 km. Summing the aftershock moment release over the aftershock cloud implies there was at least 20 cm of slip beneath the coseismic rupture over the interevent period. Beneath 10 km there were few aftershocks, indicating that any deformation was accommodated predominantly by aseismic deformation mechanisms. Notably, the amplitude of the post-seismic across-fault extension following the 2016 earthquake was 10-times smaller than following the 2011 earthquake. In the next section, we develop models of slip and stress on the Mochiyama Fault between the 2011 and 2016 earthquakes that attempt to explain these observations.

3 MODELLING STRESS CHANGES ON THE MOCHIYAMA FAULT

The observations point to three major sources of deformation in the Ibaraki–Fukushima region between the Mochiyama earthquakes: (1) post-seismic relaxation on and around the Mochiyama Fault, (2) coseismic deformation and post-seismic relaxation from the nearby Iwaki earthquakes and (3) regional post-seismic relaxation following the Tohoku-oki earthquake. Most of the GPS measurements are too far from the fault, and there are too few coherent
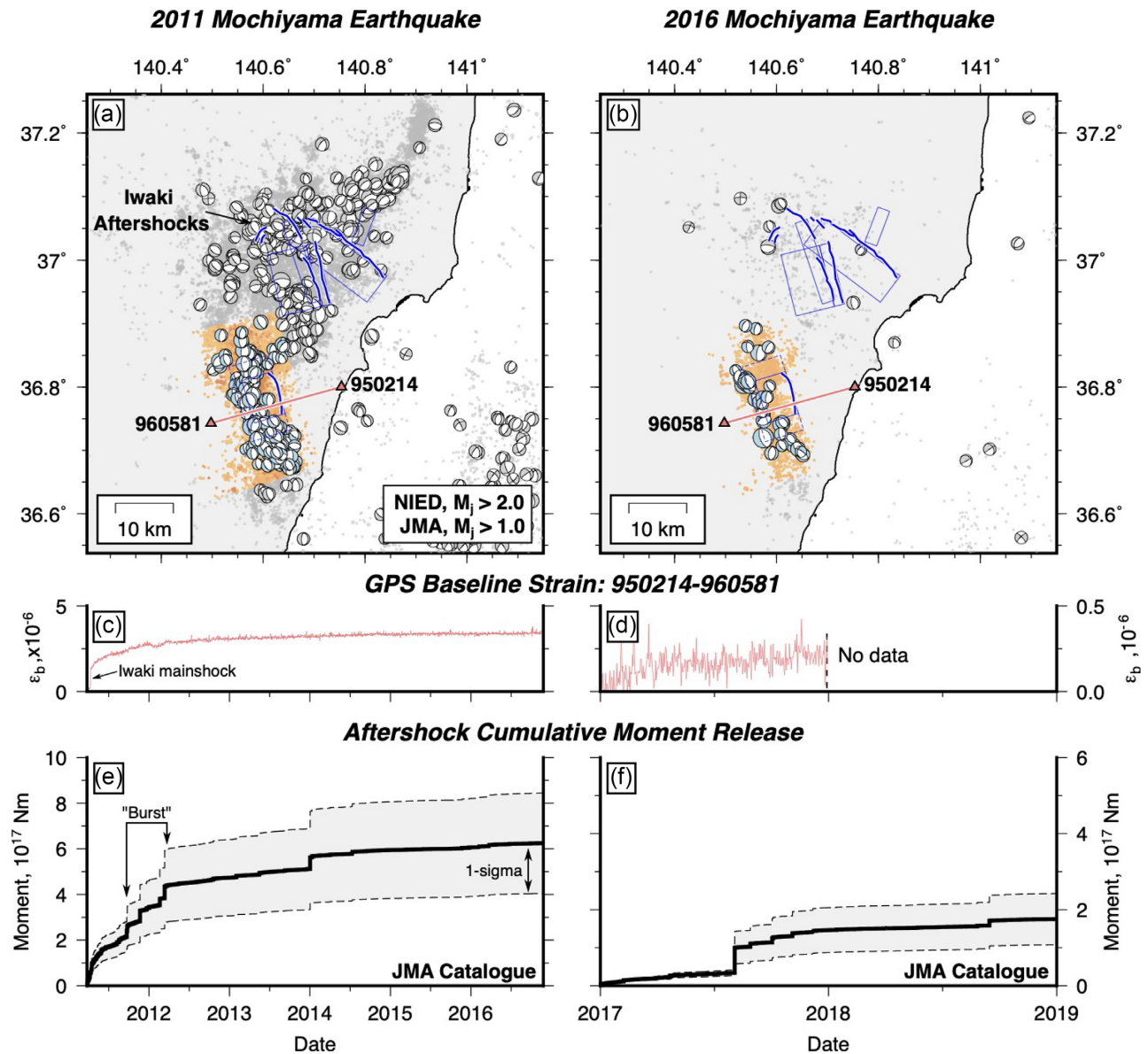
Figure 5. Locations and mechanisms of aftershocks from the JMA unified catalogue and NIED CMT catalogue following the 2011 and 2016 Mochiyama earthquakes. (a) and (b) show the map-view distribution of shallow (<20 km) seismicity relative to the Mochiyama and Iwaki Faults (blue rectangles). Events used in the moment summation in (e) and (f) are shown as gold dots. (c) and (d) show the temporal evolution of baseline strain ε_b between GEONET stations 950214 and 960581 (red triangles in a and b). Note the stark difference in the strain amplitude. (e) and (f) show the temporal evolution of cumulative moment release from aftershocks in the JMA unified catalogue. Uncertainties are shown by the dashed black lines and result from converting local magnitudes M_j to moment magnitudes M_0 using the scaling of Uchide & Imanishi (2018).

interferograms, to constrain kinematic inversions for the distribution of aseismic slip and viscous flow around the Mochiyama Fault (e.g. Murray & Segall 2002; Muto *et al.* 2019). We therefore take a forward-modelling approach to calculate how each source of deformation could have contributed to the pattern of surface strain, and the stress changes on the Mochiyama Fault, following the 2011 Mochiyama earthquake.

The time-series of deformation from the GPS and aftershock moment release indicate that the majority of the post-seismic transient visible at the surface had finished by the time of the 2016 Mochiyama earthquake, suggesting that most of the coseismic stress changes imposed on the crust surrounding the fault had been relaxed, or balanced by elastic resistance to deformation in the seismogenic layer. We therefore keep the models as general as possible

by calculating this 'fully relaxed' state, and by fitting the pattern and amplitude of strain across the Mochiyama Fault, but not the temporal evolution of the strain. Considering only the fully relaxed model has the benefit of making the estimates of reloading insensitive to the form of the constitutive laws that govern post-seismic relaxation. The calculations will, however, yield upper bounds on the amount of fault zone reloading. It is possible that some fraction of the stress changes are relaxed by deformation mechanisms with a relaxation time that is longer than the interevent period of ∼6 years, in which case the reloading will be smaller than our estimates below.

We also make the simplification that the background loading rate of the fault (the 'interseismic deformation') is small over the short time-frame between the two earthquakes, which is consistent with: (1) the lack of observed interseismic strain build around

on the Mochiyama Fault during 2005–2011 (Fig. S3a), (2) the lack of moderate-magnitude seismicity in the 50 years prior to the Mochiyama earthquakes in the gCMT catalogue (Dziewonski *et al.* 1981; Ekström *et al.* 2012) and (3) the palaeoseismic record (Komura *et al.* 2019). With these simplifications, it is the geometries of the imposed stresses and rheological components of the model domain, and the styles of post-seismic relaxation, that control the magnitude of the fault reloading.

### 3.1 Generalized models of post-seismic reloading

To first gain an understanding of how local post-seismic relaxation may have reloaded the Mochiyama Fault, we built a set of generalized stress-driven models that link coseismic slip to the post-seismic reloading of the rupture area (e.g. Ellis & Stöckhert 2004; Bagge & Hampel 2017). The models were designed to capture the maximum contribution of the three main post-seismic deformation mechanisms—afterslip, localized viscous shear and distributed viscoelastic relaxation—to reloading a normal fault after an earthquake (e.g. Freed & Lin 1998). The models also allow us to explore how uncertainties in our knowledge of the rheology of the crust and upper mantle in the study region will translate into uncertainties in the estimate of reloading of the Mochiyama Fault.

The model setup consists of a planar dip-slip fault of along-strike length L in a linear elastic layer of thickness z_e, which overlies a viscoelastic half-space (Fig. 6). The elastic layer represents the seismogenic layer in the Earth in which elastic strain can accumulate and remain stored for the duration of an earthquake cycle. The viscoelastic half-space represents the depth below which the crust and mantle is hot enough that viscous creep can relax elastic stresses over an earthquake cycle. Spatially uniform coseismic slip on the fault extends from the surface down to a depth z_r, and generates static stress changes in the surrounding medium. These static stress changes are then relaxed by viscous flow at depths $z > z_e$ and by afterslip at depths $0 \leq z \leq z_e$. In the fully-relaxed state, the afterslip zone downdip of the coseismic rupture also approximates the behaviour of a thin (<200-m wide given the model discretization) viscous shear zone surrounded by elastic wall rocks, therefore also represents the case where deformation in the lower crust is accommodated in shear zones and not by distributed flow. The coseismic rupture remains locked and cannot slip post-seismically, therefore accumulates elastic strain and is reloaded as the surrounding regions deform.

The condition for frictional failure on a fault is described by the Coulomb criterion: $\tau - \mu' \sigma = 0$, where μ' is the effective coefficient of friction, τ is the shear stress and σ is the fault-normal stress (+ve for fault clamping; Byerlee 1978). During coseismic slip the shear stress drops by $\Delta \tau_c$, whilst the normal stress change $\Delta \sigma_c$ is negligible. In order for the fault to reach its failure condition again following post-seismic stress changes $\Delta \tau_p$ and $\Delta \sigma_p$ requires the following condition to be satisfied:

$$\underbrace{\frac{\Delta \tau_p}{\Delta \tau_c} - \mu' \left(\frac{\Delta \sigma_p}{\Delta \tau_c} \right)}_{\text{Stress Changes}} + \underbrace{\Delta \mu' \left(\frac{\sigma}{\Delta \tau_c} \right)}_{\text{Strength Changes}} \simeq 1, \quad (1)$$

assuming that $\Delta \sigma_p \ll \sigma$ (see Text S2 for derivation). Eq. (1) shows that the stress changes on the fault are primarily a product of two effects: the post-seismic shear stress change relative to the coseismic shear stress drop $\Delta \tau_p / \Delta \tau_c$ (the 'shear stress recovery') and the post-seismic change in fault-normal stress relative to the coseismic shear stress drop $\Delta \sigma_p / \Delta \tau_c$ (the 'fault clamping'). Changes in the
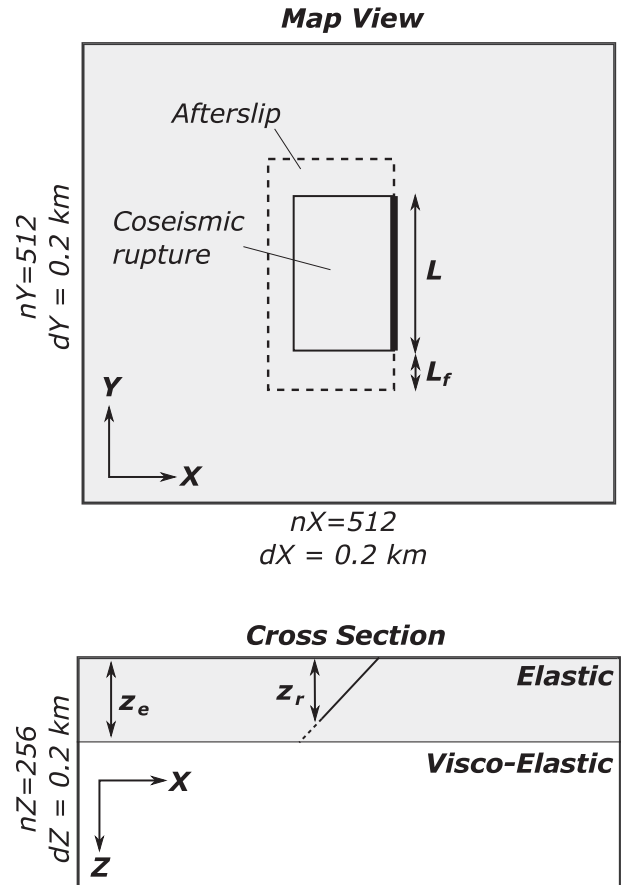
Figure 6. Sketch of the set-up of the generalized numerical calculations in map view (top panel) and cross-section (bottom panel). nX, nY and nZ are the number of nodes used in the numerical solutions, and dX, dY and dZ are the spacing between the nodes. The dashed region shows the area of the fault that can slide through post-seismic afterslip. The coseismic rupture area is discretized into eight patches along-strike and eight patches downdip.

frictional strength of the fault surface $\Delta \mu'$ may also contribute by reducing the fault stress needed for failure (the 'strength change' term in eq. 1). We evaluate the terms $\Delta \tau_p / \Delta \tau_c$ and $\Delta \sigma_p / \Delta \tau_c$ from our numerical models, and not the more common metric of Coulomb stress $(\Delta \tau_p - \mu' \Delta \sigma_p)$, to explicitly separate reloading due to changes in fault stress from the effects of fault strength. From this analysis, we can isolate the size of the strength change term, which we discuss in detail in Section 4.

We calculated $\Delta \tau_c$, $\Delta \tau_p$ and $\Delta \sigma_p$ using the Computational Infrastructure for Geodynamics code RELAX, which solves for the quasi-static deformation in elastic and viscoelastic media in response to fault slip using an equivalent body-force approach (see Barbot *et al.* 2009; Barbot & Fialko 2010a, b). We used a 102-km-wide domain with a discretization of 0.2 km to ensure that models accurately resolved the gradients in strain and stress near the edges of the coseismic rupture. Fault slip was also tapered at the margins of each fault patch to dampen stress singularities. The boundaries of the model domain were set to be at least $5L$ (~50 km) away, so that the periodicity in the solutions for displacement and stress introduced by the discrete Fourier transform that RELAX uses had little effect on the model results. After calculating the coseismic stress changes for the given coseismic slip distribution, the models were run for five relaxation times to approximate the fully relaxed state. All of the model constants are listed in Table 1.

Table 1. Parameters used in the generalized model calculations in Section 3.1.

Model parameter	Symbol	Value
Discretization	Δx_j	0.2 km
Number of nodes	N_j	512
Density	ρ	2800 kg m^{-3}
First Lamé parameter	λ	30 GPa
Shear modulus	G	30 GPa
Poisson's ratio	ν	0.25
Fault strike	θ	180°
Fault dip	δ	45°
Fault rake	ϕ	−90°

3.1.1 Results of the generalized modelling

We ran nine sets of forward calculations, varying the deformation mechanism (viscoelastic only, afterslip only and coupled afterslip + viscoelastic), the coseismic fault slip u, the depth of the coseismic rupture relative to the elastic layer thickness z_r/z_e and the along-strike length of the coseismic rupture L. We found that varying the along-strike length of fault that is able to slide through afterslip L_f had little effect on the estimates of fault reloading when $L_f > 5$ km (Fig. S6), therefore we fixed L_f to 5 km in all models. All other parameters, such as the elastic properties of the seismogenic layer, were held constant. The results of the modelling, expressed in terms of shear stress recovery $\Delta\tau_p/\Delta\tau_c$, are shown in Fig. 7. The equivalent results for the fault clamping $\Delta\sigma_p/\Delta\tau_c$ are shown in Fig. S7, but are not discussed further in the main text as they make a relatively minor ($\ll 5$ per cent) contribution to the reloading when scaled by the effective friction μ' on earthquake-generating faults (0.01–0.4; see Toda *et al.* 2011; Copley 2018; Collettini *et al.* 2019).

Models that only allow stress changes to be relaxed through viscous flow beneath the elastic layer consistently show that the shear stress recovery is largest at the base of the elastic layer and decreases non-linearly towards the surface (Figs 7a–c). Shear stress recovery is also largest within the centre of the rupture, and smallest along its edges. These first-order patterns are a result of the post-seismic strain within the elastic layer being largest at its base, where the coseismic stress changes are largest and will have driven the most viscous flow. The post-seismic strains and stress changes decay into the elastic layer, as the layer resists deformation from viscous flow below. Varying the amount of fault slip has no effect on the shear stress recovery, and varying the rupture length has only a small effect on shear stress recovery. Changing the fault slip does not alter the shear stress recovery because increasing fault slip causes a proportional increase in the amount of viscous flow needed to relax the coseismic stress change, and therefore a proportional amount of fault reloading. The depth of the rupture relative to the elastic layer thickness is the dominant control on the fault reloading, with shear stress recovery increasing significantly as the rupture depth approaches the elastic layer thickness. Nevertheless, even when the fault ruptures to the base of the elastic layer, the shear stress recovery remains less than 40 per cent of the coseismic stress drop at the base of the rupture, and less than 10 per cent at the surface.

Models that only allow stress changes to be relaxed through afterslip show a different pattern of reloading (Figs 7d–f). Shear stress recovery is largest along the edges of the coseismic rupture and within the shallowest part of the elastic layer. Again, the shear stress recovery is independent of the amount of coseismic slip, but does depend on the downdip extent of the coseismic rupture relative to the elastic layer thickness and the along-strike length of the rupture area. These patterns indicate that the larger the area that surrounds the rupture that is able to slip in response to coseismic stress changes, the more this area is able to slide post-seismically before elastic resistance from the surrounding rocks balances the stresses driving slip. Afterslip only leads to a shear stress recovery of <30 per cent of the coseismic stress drop on any particular part of the rupture.

Models that include mechanically coupled afterslip and viscoelastic relaxation generate the largest shear stress recovery on the rupture area (Figs 7g–i). Viscous flow can load the base of the coseismic rupture whilst afterslip can load the edges and top of the rupture. Shear stress recovery of 45 per cent the coseismic stress drop occurs along the edges of the rupture, whilst in the shallow part of the elastic layer the maximum shear stress recovery is 20 per cent.

These calculations demonstrate that post-seismic relaxation around the margins of a $\sim M_w$ 6 rupture can only partly reload the rupture area. Variations in the depth of the coseismic rupture relative to the thickness of the seismogenic layer, the area of the rupture and afterslip region, and the deformation mechanisms that contribute to post-seismic relaxation, will all influence the shear stress recovery, but these cannot increase the shear stress recovery beyond 45 per cent. This result is perhaps unsurprising, given that most faults rupture after hundreds to thousands of years without an earthquake, which indicates that slow interseismic strain accumulation makes up the remainder of the stress deficit on most active faults. In the next section, we apply these models to the Mochiyama earthquakes and compare them with the observed surface deformation.

3.2 Specific models of stress changes on the Mochiyama Fault

To model the stress changes specific to the Mochiyama Fault, we used the slip distribution of Fukushima *et al.* (2018) projected onto a planar approximation of the Mochiyama Fault with the geometry defined by the relocated seismicity and surface ruptures. In Section 2, we showed that the slip model of Fukushima *et al.* (2018) overestimates the amount of coseismic moment release, but the general distribution of slip is likely to be accurate given that it matches the along-strike length and across-strike width of the LOS displacement pattern measured by InSAR. We therefore scaled the amount of slip such that it matches the moment release calculated from body-waveform modelling and the coseismic strain from GPS measurements (Fig. S2). With this modification, the slip distribution has a peak slip of 0.6 m, an average shear stress drop $\Delta\tau_c$ of 3 MPa and a peak shear stress drop of 8 MPa in the centre of the rupture. The spatial variability in the stress drop is a result of high slip gradients within the core of the rupture area, and constant slip gradients along the margins of the rupture (Fukushima *et al.* 2018). We explore how uncertainties in the slip distribution could effect the estimates of fault reloading later in this section.

We calculated the post-seismic reloading of the rupture area by allowing the coseismic stress changes to be relaxed by afterslip on the main shock fault plane around the margins of the rupture, which spans the area that experienced normal-faulting aftershocks with nodal planes parallel to the main shock (Figs 5a and b). Coseismic stress changes below 10 km are either relaxed by distributed viscous flow, or by localized shear in a shear zone that follows the downdip projection of the main shock fault plane. The depth of the transition in deformation mechanism was chosen on the basis of the sharp cut-off in microseismicity at 10 km depth (Fig. S1). We consider
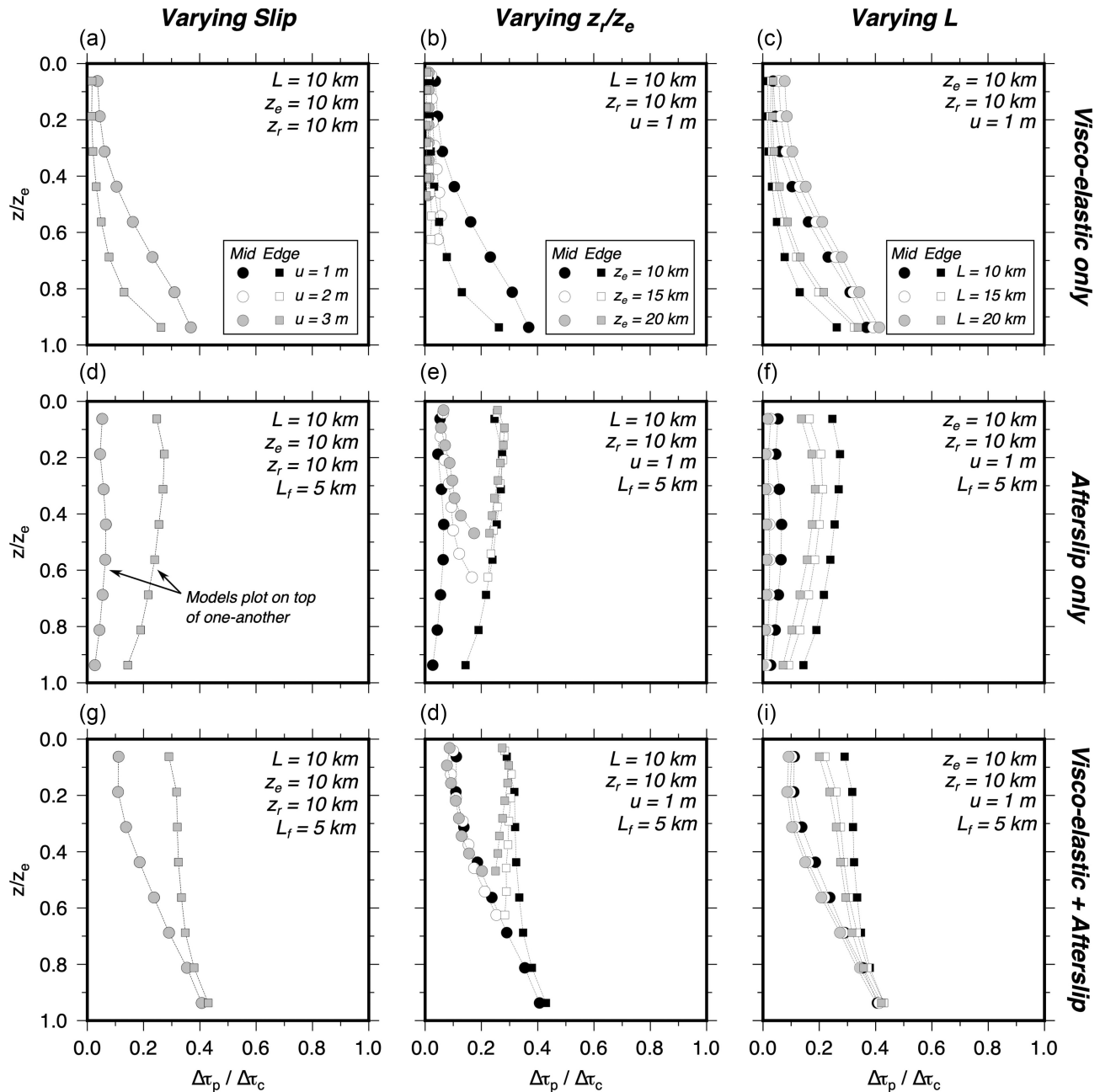
Figure 7. Results of the numerical experiments for the post-seismic shear stress recovery $\Delta\tau_p/\Delta\tau_c$ as a function of depth relative to the base of the elastic layer z/z_e when varying the amount of fault slip u (a, d, g), the depth of the fault rupture z_r (b, e, h) and the fault length L (c, f, i). The top row shows models that only include viscoelastic relaxation below $z/z_e > 1$, the middle row shows models that only include frictional afterslip above $z/z_e < 1$, and the bottom row shows models that include both viscoelastic relaxation and afterslip. Circles represent $\Delta\tau_p/\Delta\tau_c$ in the middle of the fault, whilst squares represent $\Delta\tau_p/\Delta\tau_c$ along the lateral edge of the fault. The values of the fixed parameters are shown in the top right of each box.

this elastic layer thickness to be a lower bound, and will therefore provide an upper bound on the estimate of the reloading caused by distributed viscous flow. If the elastic layer were thicker, then the estimated reloading in models that include viscous flow would be lower.

The predicted deformation is highly localized around the fault (Figs 8a and b), and only the strain measured by GPS triangles that span the fault, or are just to the south-west of the fault trace in the immediate fault hangingwall, show strain amplitudes larger than

the measurement uncertainty (0.2–0.3 microstrain). We therefore focus on comparing the modelled and observed deformation in these triangles.

Models that both include, and exclude, distributed viscous flow at depths >10 km can match the observed pattern of post-seismic strain during the interevent period, with ENE–WSW to NE–SW extension in triangles that span the Mochiyama Fault. One of the key differences between the models is that deep viscous flow generates more across-fault extension (2.6 microstrain) than if only afterslip
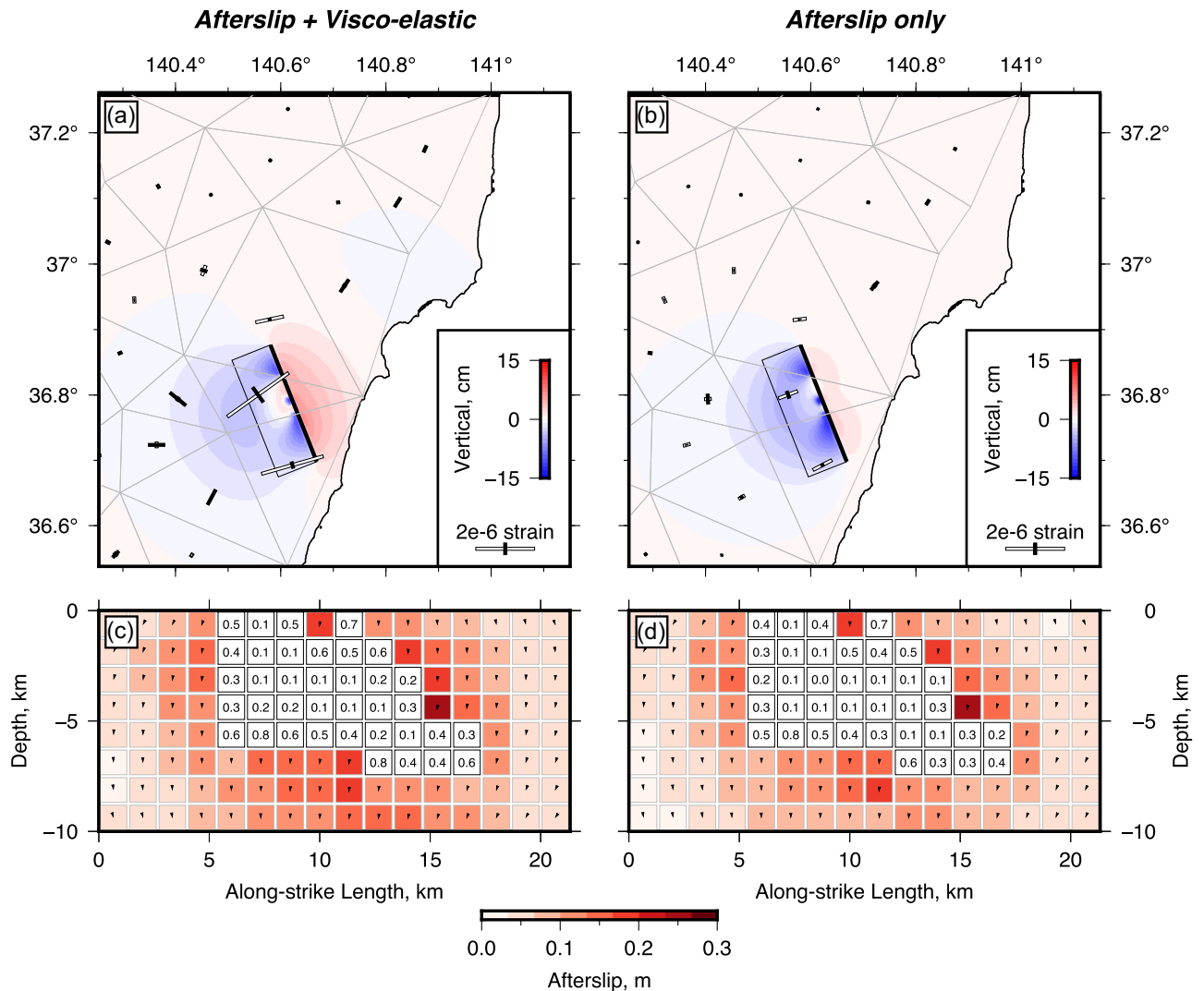
Figure 8. Stress-driven forward models of the post-seismic relaxation following the 2011 Mochiyama earthquake. (a) Vertical surface displacements and horizontal strain calculated for a model in which all of the coseismic stress changes are relaxed by afterslip and viscoelastic relaxation. The elastic layer thickness in this calculation is 10 km. (b) The same calculation as in (a), but strain is relaxed by localized shear at depths >10 km and not distributed flow. In (a) and (b) faults are marked by thin black lines, with a thick black line at their updip edge. The GPS network is shown by the light grey triangles with GPS stations at their vertices. (c) and (d) show the distribution of afterslip and the shear stress recovery $\Delta\tau_c/\Delta\tau_p$ on the coseismic rupture. Arrows on each afterslip patch show the slip vector and are scaled by the afterslip amplitude.

and localized viscous shear are allowed to relax the coseismic stress changes (0.7 microstrain). This difference reflects the fact that distributed flow at depth produces long-wavelength surface deformation that strongly affects the GPS sites that are 10–20 km from the fault. Nevertheless, both models still underestimate the total amount of interevent extension observed across the Mochiyama Fault (3.1–3.6 microstrain). GPS triangles to the southwest of the fault trace within the fault hangingwall show different patterns of strain for the different mechanisms of post-seismic relaxation at depth. Afterslip beneath the rupture produces a small amount of incremental NE–SW extension, whilst distributed viscous flow produces incremental contraction that rotates in orientation from north to south that is more consistent with the observed pattern of interevent strain (Figs 8a and b).

Despite the differences in the predicted surface strain, the models yield similar patterns of afterslip and fault reloading, with up to

80 per cent shear stress recovery along the margins of the rupture and less than 10 per cent within its interior (Figs 8c and d). The shear stress recovery along the margins of the rupture area is larger than in the spatially uniform slip models shown in Section 3.1, because the margins of the rupture have a low coseismic stress drop when calculated using the distributed slip model, yet experience the largest post-seismic stress changes. The shear stress recovery averaged over the rupture for models with and without viscoelastic relaxation are 33 and 28 per cent, respectively, which is consistent with the average shear stress recovery in the generalized models that use a similar rheological structure (Figs 7e and h). As seen in the Section 3.1, viscous flow at depth has little effect on the shear stress recovery, because the fault did not rupture all the way to the base of the elastic layer. The modelled fault clamping $\Delta\sigma_p/\Delta\tau_c$ is everywhere <10 per cent (Fig. S8), and therefore makes a negligible contribution to the reloading when scaled by the effective friction.
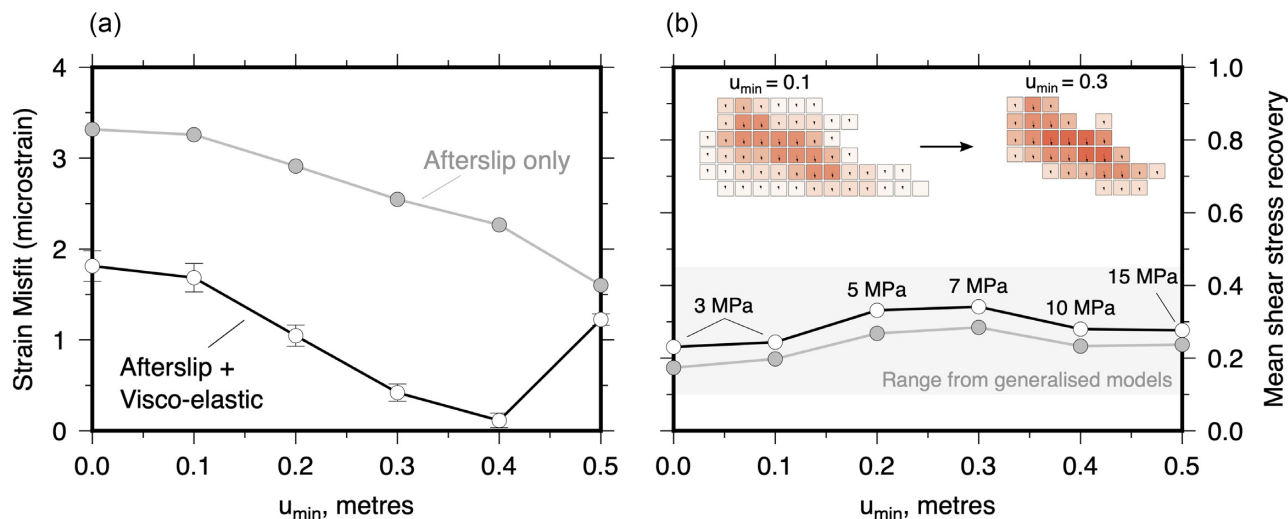
Figure 9. Calculations showing the effect of compacting the slip distribution on the observed surface strain and shear stress recovery. (a) Misfit between the observed and modelled across-fault extensional strain as a function of u_{min}. The misfit is calculated as: $1/n_j \sum_j \left[(\varepsilon_{min}^{mod} - \varepsilon_{min}^{obs})^2 \right]^{1/2}$, where ε_{min}^{mod} is the modelled minimum principal strain amplitude and ε_{min}^{obs} is the observed minimum principal strain amplitude in the triangles $j = \{1, 2,..., n_j\}$ that span the Mochiyama Fault. Error bars are ± 0.3 microstrain, but are not shown for the afterslip-only models. (b) Mean shear stress recovery over the whole rupture area. The grey background is the range of shear stress recovery inferred from the generalized models. Numbers above each point represent the fault-averaged stress drop for the slip model used to calculate the coseismic stress changes. Examples of the slip models are shown in the top half of the figure for $u_{min} = 0.1$ m and $u_{min} = 0.3$ m.

3.2.1 Effects of the coseismic slip distribution on reloading

The stress changes that drive post-seismic relaxation are a function of gradients in the input slip model. Therefore, the smoothing used to regularize the inversions for coseismic slip, or the inclusion of some post-seismic slip in the coseismic slip distribution, may have an effect on the predicted amplitude of post-seismic deformation. To explore whether this effect can account for the difference between the modelled and observed interevent strain across the Mochiyama Fault, we ran a series of calculations in which we artificially vary the smoothing of the input slip distribution in the 2011 earthquake by removing areas with slip less than some minimum value u_{min}, and then redistribute the remaining moment release evenly across the rupture area (e.g. Barbot *et al.* 2009). This process leads to a compaction of the slip distribution, and an increase in the coseismic stress drop (Fig. S9), with a slight decrease in the fit between the observed and modelled coseismic surface deformation.

Models with more compact slip distributions and higher stress drops cause more post-seismic relaxation and larger surface strains (Fig. 9a). If all areas with slip <0.4 m are removed, which adjusts the average stress drop to be 10 MPa, then the models can account for the observed 3.1–3.6 microstrain of across-fault extension over the interevent period. Nevertheless, compacting the slip distribution has little effect on the average shear stress recovery on the rupture (Fig. 9b), because the coseismic stress drop also increases. The generalized calculations in Section 3.1.1 provide the physical explanation for this feature of the models: increased stress drop causes increased elastic strain within the surrounding crust, which itself leads to a proportional amount of fault zone reloading through post-seismic relaxation. Therefore, although uncertainties in the roughness of the slip distribution of the 2011 earthquake can account for the discrepancy between the modelled and observed across-fault strain between the 2011 and 2016 Mochiyama earthquakes, the rupture area can still only be reloaded by on average ≲35 per cent of the coseismic stress drop through post-seismic relaxation (Fig. 9b). A high coseismic stress drop also does not

account for the significant difference in the amplitude of the post-seismic strain observed following the 2011 and 2016 Mochiyama earthquakes. In the next section, we explore what contributions the static and time-dependent stress changes from the Iwaki earthquake sequence could have made to the reloading of the Mochiyama Fault.

3.2.2 Stress changes from the Iwaki earthquakes

We used the fault geometry and slip estimates from Fukushima *et al.* (2013) to calculate the co- and post-seismic displacements due to slip in the Iwaki earthquake sequence, and the resulting stress changes on the Mochiyama Fault. The modelled coseismic strain matches the strain observed by the GPS network, and can account for the 0.7 microstrain of extension across the Mochiyama Fault in April 2011 (Fig. S10). We find that the Iwaki earthquakes caused a <0.3–0.4 MPa increase in shear stress (Fig. 10b) and a <0.2–0.3 MPa decrease in normal stress (Fig. 10c) along the northern-most portion of the Mochiyama Fault. The amplitude of these static stress changes decrease significantly towards the southern edge of the Mochiyama Fault, as stress decays as the inverse cube of distance from the strain source in the elastic crust (Okada 1992). Therefore, although the Iwaki earthquakes did move the Mochiyama Fault closer to failure, they contributed a shear stress recovery of <5–10 per cent of the coseismic stress drop (3–10 MPa; Fig. 10a).

Post-seismic relaxation on the Iwaki Faults could have produced up to 0.3–0.5 microstrain of extension across the Mochiyama Fault, which is ∼10–15 per cent of the observed interevent extension. The stress changes oppose the initial static loading with a shear stress decrease of <0.2–0.3 MPa (Fig. 10d) and a normal stress increase of <0.3–0.4 MPa (Fig. 10e) along the base of the Mochiyama Fault. Models that do not include distributed viscous flow below 10 km depth predict negligible strain and stress changes on the Mochiyama Fault that are ≪0.1 MPa (Fig. S11). Mechanically coupled models that include the co- and post-seismic stress changes in both
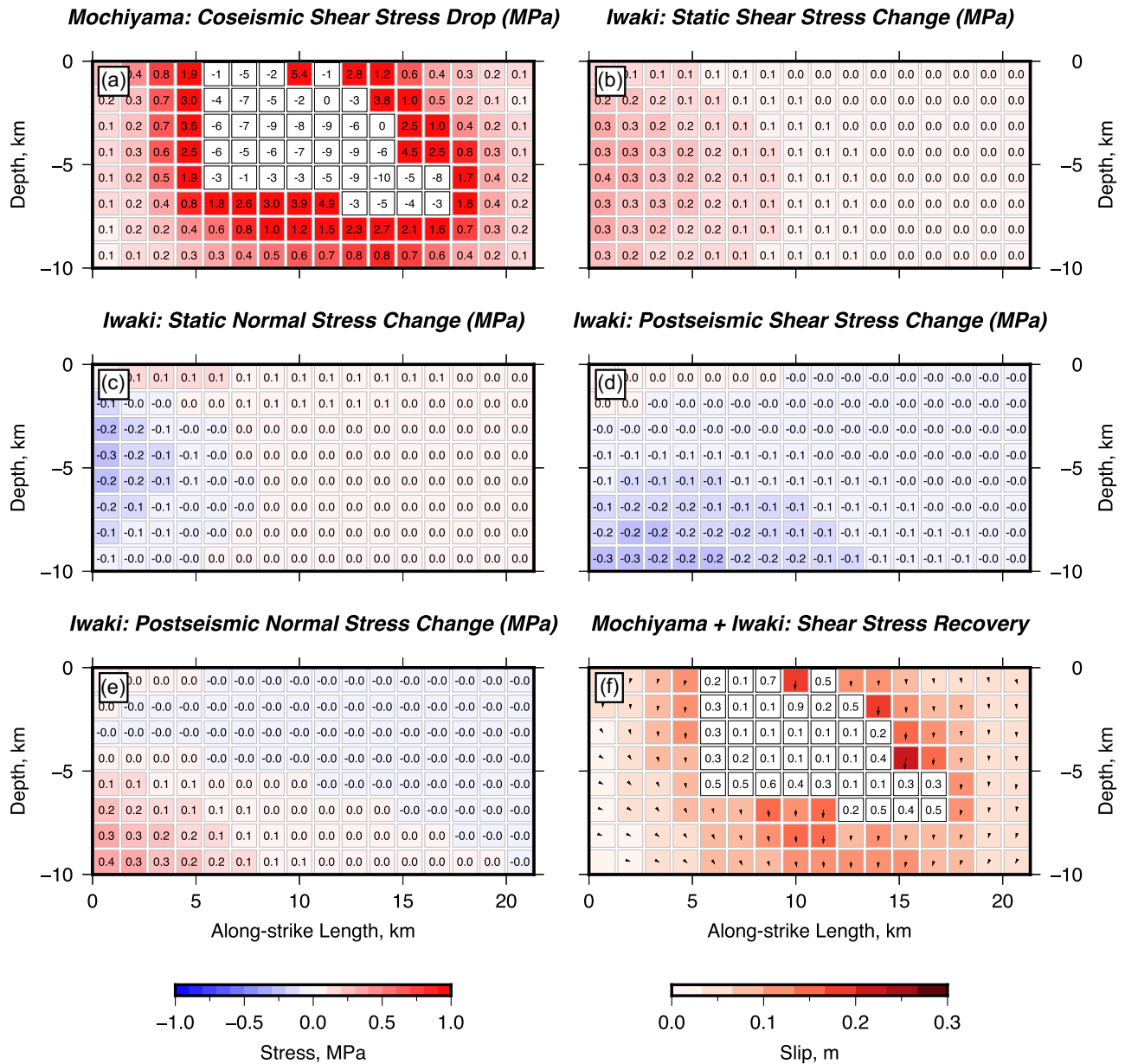
Figure 10. Contribution of the static deformation and post-seismic relaxation associated with the Iwaki earthquakes to reloading of the Mochiyama Fault. By convention, shear stress changes are positive if the fault is loaded in the direction of slip and normal stress changes are positive for fault clamping. (a) Coseismic shear stress changes from slip on the Mochiyama Fault only. Shear stress (b) and normal stress (c) changes on the Mochiyama Fault due to coseismic slip in the Iwaki earthquakes. Shear stress (d) and normal stress (e) changes due to post-seismic relaxation following the Iwaki earthquakes. (f) The pattern of afterslip and shear stress recovery on the Mochiyama Fault due to the relaxation of coseismic stress changes in models that include slip on both the Mochiyama and Iwaki faults. Colour scale for afterslip is the same as that in Fig. 8.

events show that the Iwaki earthquakes will have only slightly inhibited afterslip on the northern half of the Mochiyama Fault, and could have reduced the average shear stress recovery by <2 per cent (Fig. 10f). Therefore, despite the proximity of the Iwaki earthquakes to Mochiyama, the static and time-dependent stress changes caused by the Iwaki earthquake sequence played a minor role in the reloading the Mochiyama Fault.

3.2.3 Stress changes from the Tohoku-oki earthquake

Coseismic slip in the 11th March 2011 Tohoku-oki earthquake horizontally stretched the overriding plate and caused widespread changes in the style and frequency of seismicity in the shallow crust of mainland Japan (Okada *et al.* 2011). Seismicity in the study region prior to the Tohoku-oki earthquake consisted mostly of normal faulting (Imanishi *et al.* 2012), and the static stress changes from the Tohoku-oki earthquake were equivalent to a shear stress increase of 0.8 MPa and a normal stress drop of −1.2 MPa on the Mochiyama Fault [calculated from the model of Hu *et al.* (2016)]. These stress changes did not immediately trigger rupture, but likely brought the Mochiyama Fault close to failure. Post-seismic relaxation following the Tohoku-oki earthquake contributed additional loading of faults in mainland Japan (Becker *et al.* 2018). Fukushima *et al.* (2018) calculated that afterslip on the megathrust around the Tohoku-oki

rupture area would have subject the Mochiyama Fault to an increase in shear stress of 0.1 MPa and a decrease in fault normal stress of −0.2 MPa over the period March 2011 to December 2016. A more complex calculation by Hu *et al.* (2016), which includes the effects of viscoelastic relaxation beneath the crust, afterslip on the megathrust and interseismic relocking of the subduction interface, suggests there may have been a shear stress increase of 0.07 MPa and a normal stress drop of −0.2 MPa on the Mochiyama Fault over the same period (Fig. S12). Both models predict stress changes that are small compared to the coseismic stress drop in the Mochiyama earthquake, and would directly contribute to ≪5 per cent of the shear stress recovery on the rupture area.

The stress changes from the Tohoku-oki earthquake will have also influenced the pattern and amplitude of afterslip around the rupture area on the Mochiyama Fault (Fukushima *et al.* 2018). We ran calculations that include the relaxation of both the coseismic stress changes due to the Mochiyama earthquake through localized afterslip, and the co- and post-seismic stress changes from the Tohoku-oki earthquake in the model of Hu *et al.* (2016) resolved on the Mochiyama Fault. We include the coseismic stress changes from the Tohoku-oki earthquake, as it is unlikely that a significant fraction of this stress imposed on the Mochiyama Fault was relaxed by the timing of the 2011 Mochiyama earthquake given that they were only 7 days apart. These calculations produce up to 2.0 microstrain of extension across the Mochiyama Fault by boosting the average amount of afterslip around the rupture area from ∼20 to ∼60 cm (Fig. 11a). However, the orientations of the minimum principal strain axes in triangles that span the Mochiyama Fault are rotated anticlockwise relative to strain axes measured by the GPS network, and the maximum principal strain axes in triangles in the fault hangingwall do not match the observed ∼ENE–WSW contraction in these areas. These differences between the stress-driven models and observations can be accounted for if afterslip were constrained to have a similar rake to coseismic slip and occurred mostly on the top ∼5 km of the Mochiyama Fault (Figs 11c and d).

The relaxation of stress changes caused by the Tohoku-oki earthquake by slip on the Mochiyama Fault (Fig. 11a), along with the co- and post-seismic deformation in the nearby Iwaki earthquakes (Fig. S10), can therefore account for the majority of the extension measured by the GPS network over the interevent period, and the order-of-magnitude difference in the amplitude of post-seismic strain observed following the 2011 and 2016 Mochiyama earthquakes. When including the additional deformation caused by the stress changes in the Tohoku-oki earthquake, the average shear stress recovery on the main shock rupture area increases to 40 per cent, which is still only a fraction of that needed to entirely reload the rupture to its former failure stress.

3.2.4 Effects of a pre-stress or triggered slip on reloading

Pre-existing stresses around the rupture area on the Mochiyama Fault may have also been relaxed by aseismic slip or localized aseismic shearing within the downdip shear zone during the interevent period. Any pre-existing stresses would require some mechanism that allows elastic strain to be stored in the wall rocks around the edge of the rupture area without being relaxed by aseismic slip or during slip in the Mochiyama earthquakes, similar to the mechanism that generates slow-slip events (Bürgmann 2018). These stresses could have driven more deformation than would be predicted by a model in which only coseismic stress changes are considered, and could have led to increased reloading of the rupture area. The

kinematic forward models in Fig. 11 demonstrate that any shallow triggered slip caused by the relaxation of pre-existing stresses would generate extension in triangles that span the fault and contraction within the fault hangingwall (Fig. 11c). Deep slip, on the other hand, would generate mostly extensional strain within the fault hangingwall (Fig. 11d). The GPS measurements of interevent strain can therefore be used to place a bound on the amplitude of deep and shallow triggered slip, and the associated shear stress recovery. A more complex model of distributed fault slip would be poorly constrained by the GPS observations.

We performed a grid search of models in which we imposed slip around the edge of the coseismic rupture on the shallow (<5 km) and deep (5–10 km) sections of the Mochiyama Fault, and evaluated the fit between the models and the strain observations (Fig. 12). The model that best fits the observed interevent strain has 80 cm of shallow afterslip and 20 cm of deep afterslip (see Fig. S13 for a comparison between this kinematic model and the best-fitting stress-driven models). We also found that the amplitude of shallow triggered slip is limited to 60–90 cm in order to account for the amplitude of the across-fault fault extension during the interevent period. For this amount of shallow slip, there cannot have been more than 30–40 cm of triggered slip or localized viscous shear beneath the coseismic rupture, as this would produce extensional strain within the fault hangingwall that is not consisted with the observed strain. These constraints on the amplitude of shallow and deep triggered slip limit the shear stress recovery that could have been caused by the relaxation of pre-existing stresses to 50–80 per cent of the coseismic stress drop (3–10 MPa; Fig. 12).

4 DISCUSSION

4.1 Surface strain and stress changes on the Mochiyama Fault

Our modelling demonstrates that post-seismic relaxation driven by coseismic stress changes can account for the pattern and amplitude of the strain observed across the Mochiyama Fault if the stress drop in the earthquake was at least 10 MPa and all of the coseismic stress changes were relaxed by creep and viscous flow in the interevent period. As the stress changes on the rupture area of the Mochiyama Fault caused by post-seismic relaxation are proportional to the coseismic stress drop, however, a higher stress drop does not equate to a higher shear stress recovery. Models that only include the relaxation of the coseismic stress changes in the 2011 Mochiyama earthquake, and that match the observed interevent strain, recover only 35 per cent of the fault-averaged coseismic shear stress drop, or less.

Although these models can account for the amplitude of the observed deformation, they cannot account for a number of other observations from the Ibaraki–Fukushima earthquake sequence. First, such a stress drop would require average differential stresses within the top 10 km of the crust of at least 20 MPa. It is unlikely the differential stresses exceed a few tens of MPa, given the widespread change in the mechanisms of earthquakes in mainland Japan following the relatively minor (<1–2 MPa) stress changes caused by the Tohoku-oki earthquake (Wang *et al.* 2019). Secondly, the assumption that all of the coseismic stress change imposed on the mid-lower crust was relaxed over the 6-year-interevent period would require an effective viscosity of ≲10^{18} Pa s at 10–40 km depth. Such effective viscosities are far lower than those derived from matching geodetic measurements of the response of the crust to stress changes in large
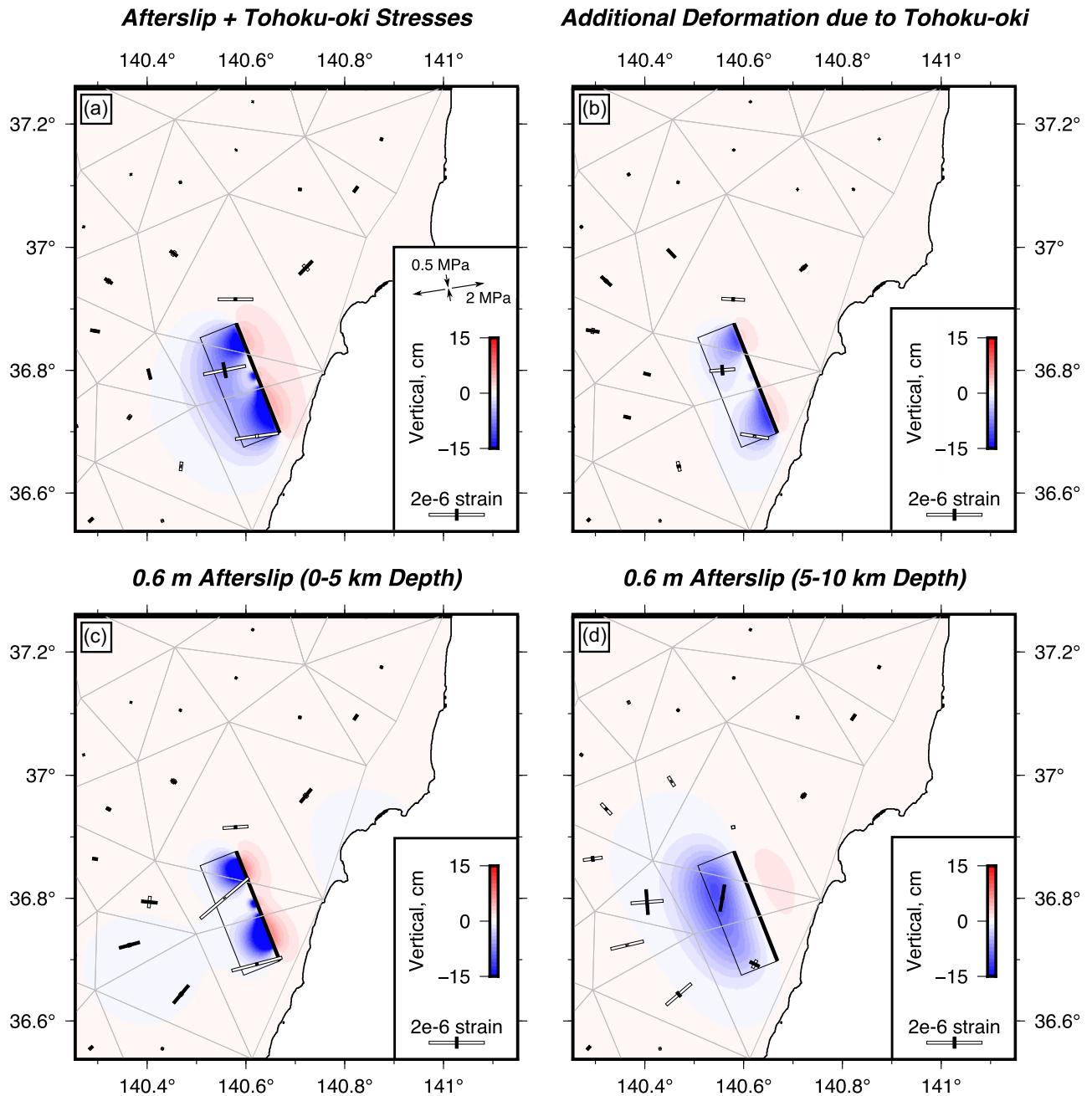
Figure 11. Effect of the Tohoku-oki earthquake on the post-seismic deformation around the Mochiyama Fault. (a) Surface strain predicted by a model in which both the coseismic stress changes due to slip in the 2011 Mochiyama earthquake, and the stress changes due to co- and post-seismic deformation from the Tohoku-oki earthquake, are relaxed by slip on the Mochiyama Fault. The principal stress changes caused by co- and post-seismic deformation in the Tohoku-oki earthquake from the model of Hu *et al.* (2016) are shown in the legend. (b) Difference between the model in (a) and the model in Fig. 8b, showing the additional surface deformation caused by the Tohoku-oki earthquake. (c) Forward model of the strain predicted for 0.6 m of shallow afterslip on the top 5 km of the Mochiyama Fault around the edges of the coseismic rupture. The rake of the afterslip is in the same direction to coseismic slip. (d) Same as (c) but for 0.6 m of slip in the bottom 5 km of the Mochiyama Fault. (c) and (d) show that, to account for the observation of contractional strain within GPS triangles in the fault hangingwall over the interevent period, the majority of the afterslip must have been relatively shallow.

megathrust earthquakes ($\sim 10^{19}$–10^{21} Pa s; see Thatcher *et al.* 1980; Muto *et al.* 2019). Incomplete relaxation of the coseismic stress changes through viscous flow in the mid-lower crust would lead to less reloading than our estimates (i.e. <40 per cent of the coseismic stress drop of 3–10 MPa). Finally, relaxation of only coseismic stress changes cannot account for the order-of-magnitude difference in the amplitude of the deformation observed following 2011 and 2016 earthquakes, suggesting some other stress contribution

is needed to explain this feature of the post-seismic deformation around the Mochiyama Fault.

The static stress changes due to the nearby Iwaki earthquakes moved the Mochiyama Fault closer to failure, but recovered only <10 per cent of the stress drop in the 2011 Mochiyama earthquake. Subsequent post-seismic relaxation will have unloaded the Mochiyama Fault and moved it further from failure. Therefore, the stress changes caused by the nearby Iwaki earthquake sequence had

Kinematic Forward Models
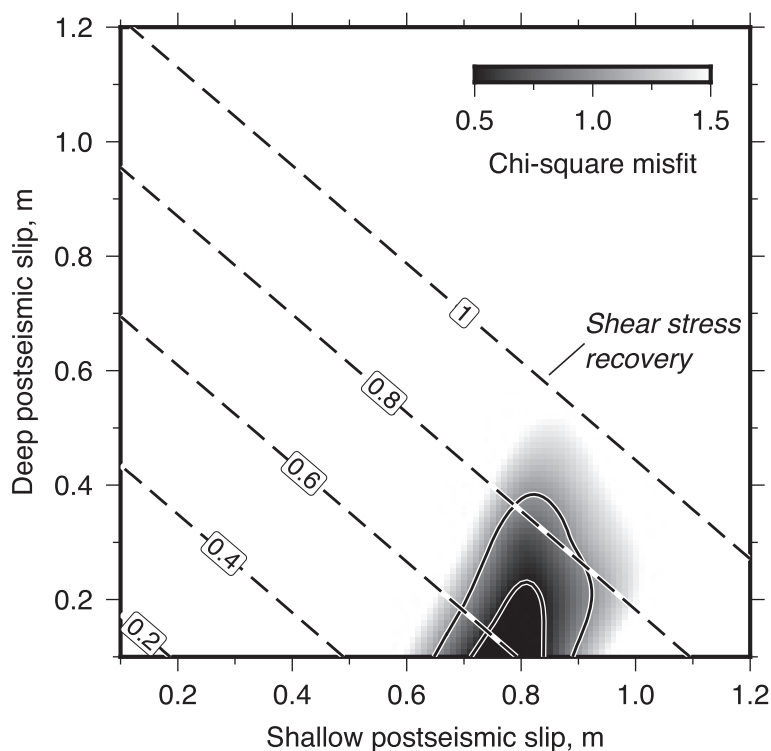
Figure 12. Kinematic forward models for the amount of shallow and deep triggered slip needed to account for the interevent strain observations. The misfit between the models and the observations is expressed as the chi-squared misfit (χ^2), which is calculated as: $\chi^2 = 1/N \sum_{ij} \left[(\varepsilon_{ij}^{obs} - \varepsilon_{ij}^{mod})/\sigma \right]^2$, where $i = \{xx, xy, yy\}$ is the strain component, $j = \{1, 2,..., n_j\}$ is the strain triangle, $N = 3n_j$ and σ is the uncertainty that we take to be 0.3 microstrain. We calculate the misfit for triangles that span the fault and that are within the fault hangingwall. The solid black lines represent the $\chi^2 = 0.5$ and $\chi^2 = 1.0$ contours. The dashed black lines show the mean shear stress recovery on the rupture area for the given amount of shallow and deep triggered slip. Models that match the observed strain have predominantly shallow slip, and an average shear stress recovery between 50 and 80 per cent of the shear stress drop.

a small effect on reloading the Mochiyama Fault in comparison to the localized post-seismic relaxation around the margins of the coseismic rupture, and cannot account for the differences between the post-seismic deformation after the 2011 and 2016 Mochiyama earthquakes.

The Tohoku-oki earthquake, and its post-seismic deformation, could have increased the amount of afterslip on the Mochiyama Fault and brought the rupture area closer to failure. Models that include these effects can account for the amplitude of the measured across-fault extension in the interevent period and the order-of-magnitude difference in the amplitude of the across-fault extension observed following the 2011 and 2016 Mochiyama earthquakes. However, the inference of Fukushima *et al.* (2018) that this additional afterslip on the Mochiyama Fault reloaded it back to its former failure stress is inconsistent with our model results. We instead find that the rupture area on the Mochiyama Fault could only have been reloaded by less than half of the coseismic shear stress drop by the time of the 2016 earthquake.

Alternatively, over the interevent period (2011–2016), there may have been some triggered slip around the rupture area on the Mochiyama Fault that relaxed pre-existing stresses. The GPS data cannot differentiate between coseismic stress-driven afterslip, or triggered slip that does not correlate with coseismic stress changes. Nevertheless, we find that triggered slip cannot have led to a shear stress recovery larger than 50–80 per cent of the coseismic shear

stress drop, and again would not have been able to entirely reload the rupture on the Mochiyama Fault. This mechanism also seems unlikely, given that it needs enough elastic strain to have been stored around the margins of the rupture area to generate nearly twice as much post-seismic slip than there was coseismic slip in the 2011 Mochiyama earthquake. We therefore conclude that the stresses needed to break the fault in earthquakes must have decreased through time to account for the short interevent time between the 2011 and 2016 Mochiyama earthquakes by at least 1–5 MPa (50–80 per cent of the stress drop; Fig. 13).

4.2 Time-dependent decrease in fault strength

Most active faults do not experience such short interevent times between moderate-magnitude earthquakes, suggesting that the mechanisms that decreased the strength and changed the stresses on the Mochiyama Fault between 2011 and 2016 were unusual. The static strength of a fault's surface can be described by the effective frictional resistance to slip $\mu' = \mu(1 - \lambda)$, where μ is the intrinsic friction and $\lambda = P_f/\sigma$, where Pf is the pore-fluid pressure on the fault (Hubbert & Rubey 1959). The drop in fault strength may therefore have been due to a decrease in the intrinsic friction of the material making up the fault surface, or an increase in the pore-fluid pressure within the fault core.

Sketch of the Average Shear Stress Evolution on the Mochiyama Fault
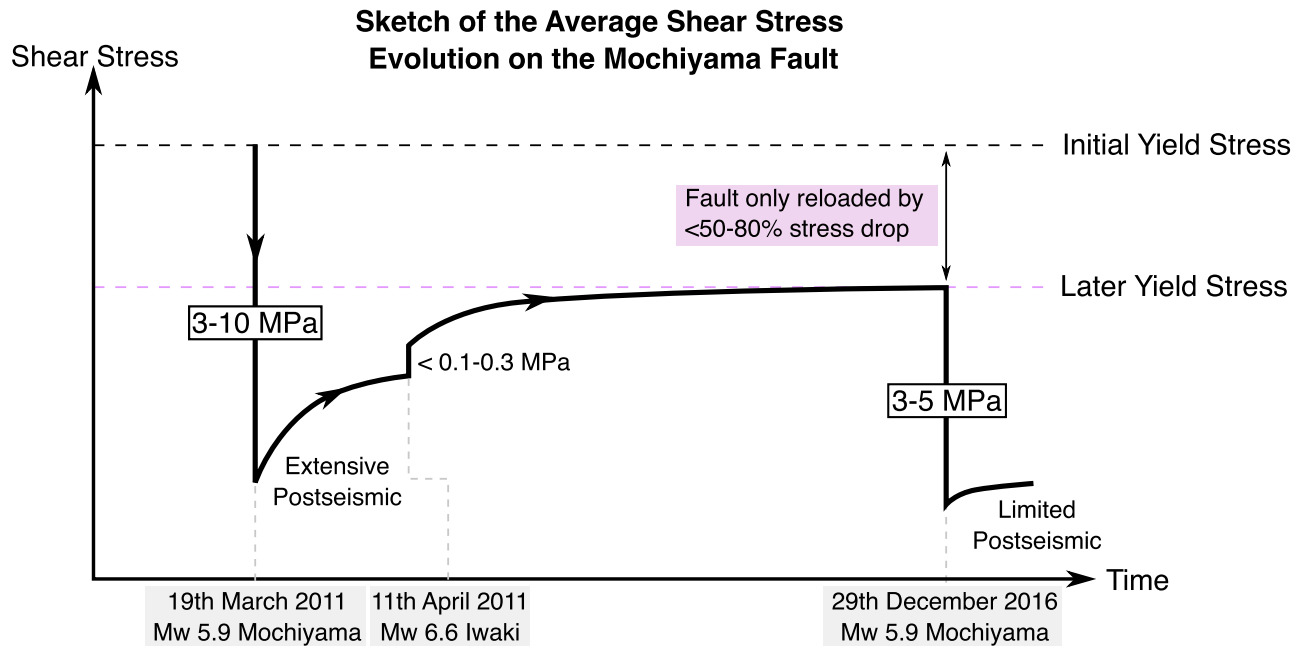
Figure 13. Sketch of the evolution of the fault-averaged shear stress on the Mochiyama Fault between the 2011 and 2016 earthquakes. The stress drop in the 2011 earthquake and 2016 earthquakes are shown in black boxes, and were calculated from the slip distributions of Fukushima *et al.* (2018).

One possibility is that the fault strength decreased immediately following the 2011 Mochiyama earthquake as a result of the frictional slip weakening commonly observed in laboratory experiments (e.g. Dieterich 1979; Ikari *et al.* 2013) and failed to recover back to its former level. In this situation, it may have been the unusually fast reloading of the Mochiyama Fault relative to the slow rate of strength recovery that led to the unusually short interevent time. The high rate of stress recovery was most likely a result of enhanced post-seismic deformation around the Mochiyama Fault that relaxed the co- and post-seismic stress changes following the 2011 Mochiyama and Tohoku-oki earthquakes.

Alternatively, the fault may have experienced a more steady decrease in strength. Vertical migration of high-pressure fluids through the shallow crust in mainland Japan following the Tohoku-oki earthquake has been widely invoked to account for migrating seismicity (Yoshida *et al.* 2015, 2017, 2020), temporal changes in the shallow shear wave velocity structure (Wang *et al.* 2021) and groundwater geochemistry around crustal faults (Sato *et al.* 2020). Infiltration of fluid onto the rupture area of the Mochiyama Fault could have reduced the average shear stresses needed for failure, whilst also promoting aftershock seismicity, by changing the effective fault-normal stresses (Hainzl 2004). We did not find any evidence for the spatial migration of earthquake hypocentres around the Mochiyama Fault that might reflect a fluid front causing small patches of the fault to fail sequentially (Fig. S14; e.g. Shapiro *et al.* 1997; Walters *et al.* 2018). Any fluid infiltration onto the fault zone also did not affect the timescale over which coseismic stress changes were relaxed, as the post-seismic transients after the 2011 and 2016 Mochiyama earthquakes followed similar temporal decays. Therefore the mechanism(s) that decreased the strength of the Mochiyama Fault had surprisingly little effect on the geodetic or microseismic observations during the interevent period, other than the highly energetic aftershock sequence beneath the main shock rupture area (see Section 2.4).

5 CONCLUSION

We have demonstrated that earthquake-related stress changes and their post-seismic relaxation can explain the pattern of strain measured by Japan's GPS network during the 2011–2016 Mochiyama earthquakes in the Ibaraki–Fukushima region. Models that match the observed interevent strain can only reload the rupture area on the fault by less than 50–80 per cent of the fault-averaged coseismic stress drop (3–10 MPa), irrespective of the rheological structure of the crust and mantle, or the mechanisms of post-seismic relaxation. We conclude that the Mochiyama Fault experienced a drop in its effective strength, and the shear stresses needed to break the fault reduced by at least 1–5 MPa. The mechanism(s) that caused this weakening are unclear, but appear to have been associated with an unusually energetic aftershock sequence around the margins of the coseismic rupture. Time-dependent changes in fault strength may therefore play a role in modulating the timing of moderate-magnitude earthquakes, but may be difficult to detect using geodetic and microseismicity observations.

DATA AVAILABILITY

All data and code used in this study are freely available online. The GPS data used in this study are available from https://www.gsi.go.jp/ENGLISH/geonet_english.html (last accessed July 2022). The JMA microseismicity data are available from https://www.data.jma.go.jp/svd/eqev/data/bulletin/index_e.html (last accessed March 2021) and the NIED earthquake moment tensors are available from https://www.fnet.bosai.go.jp/fnet/event/search.php (last accessed March 2021). The Envisat and Sentinel-1 data are freely accessible through ESAs Copernicus Schihub https://scihub.copernicus.eu/ (last accessed January 2022). The numerical model RELAX is available from https://geodynamics.org/cig/software/relax/ (last accessed March 2021).

REFERENCES

Bagge, M. & Hampel, A., 2017. Postseismic Coulomb stress changes on intra-continental dip-slip faults due to viscoelastic relaxation in the lower crust and lithospheric mantle: insights from 3D finite-element modelling, *Int. J. Earth Sci.,* **106**(8), 2895–2914.

Barbot, S. & Fialko, Y., 2010a. A unified continuum representation of post-seismic relaxation mechanisms: semi-analytic models of afterslip, poroelastic rebound and viscoelastic flow, *Geophys. J. Int.,* **182**(3), 1124–1140.

Barbot, S. & Fialko, Y., 2010b. Fourier-domain Green's function for an elastic semi-infinite solid under gravity, with applications to earthquake and volcano deformation, *Geophys. J. Int.,* **182**(2), 568–582.

Barbot, S., Fialko, Y. & Bock, Y., 2009. Postseismic deformation due to the Mw 6.0 2004 Parkfield earthquake: stress-driven creep on a fault with spatially variable rate-and-state friction parameters, *J. geophys. Res.,* **114**(B7), doi:10.1029/2008JB005748.

Becker, T.W., Hashima, A., Freed, A.M. & Sato, H., 2018. Stress change before and after the 2011 M9 Tohoku-oki earthquake, *Earth planet. Sci. Lett.,* **504**, 174–184.

Bedford, J.R., Moreno, M., Deng, Z., Oncken, O., Schurr, B., John, T., Báez, J.C. & Bevis, M., 2020. Months-long thousand-kilometre-scale wobbling before great subduction earthquakes, *Nature,* **580**(7805), 628–635.

Bourne, S.J., Árnadóttir, T., Beavan, J., Darby, D.J., England, P.C., Parsons, B., Walcott, R.I. & Wood, P.R., 1998. Crustal deformation of the Marlborough Fault Zone in the South Island of New Zealand: geodetic constraints over the interval 1982-1994, *J. geophys. Res.,* **103**(B12), 30 147–30 165.

Bürgmann, R., 2018. The geophysics, geology and mechanics of slow fault slip, *Earth planet. Sci. Lett.,* **495**, 112–134.

Byerlee, J., 1978. Friction of rocks, *Pure appl. Geophys.,* **116**(4–5), 615–626.

Cheloni, D. *et al.*, 2010. Coseismic and initial post-seismic slip of the 2009 Mw 6.3 L'Aquila earthquake, Italy, from GPS measurements, *Geophys. J. Int.,* **181**(3), 1539–1546.

Christensen, D.H. & Ruff, L.J., 1985. Analysis of the trade-off between hypocentral depth and source time function, *Bull. seism. Soc. Am.,* **75**(6), 1637–1656.

Churchill, R.M., Werner, M.J., Biggs, J. & Fagereng, Å., 2022. Afterslip moment scaling and variability from a global compilation of estimates, *J. geophys. Res.,* **127**(4), e2021JB023897, doi:10.1029/2021JB023897.

Collettini, C., Tesei, T., Scuderi, M.M., Carpenter, B.M. & Viti, C., 2019. Beyond Byerlee friction, weak faults and implications for slip behavior, *Earth planet. Sci. Lett.,* **519**, 245–263.

Copley, A., 2018. The strength of earthquake-generating faults, *J. Geol. Soc.,* **175**(1), doi:10.1144/jgs2017-037.

Dieterich, J.H., 1979. Modeling of rock friction 1. Experimental results and constitutive equations, *J. geophys. Res.,* **84**(B5), 2161–2168.

Dziewonski, A.M., Chou, T.-A. & Woodhouse, J.H., 1981. Determination of earthquake source parameters from waveform data for studies of global and regional seismicity, *J. geophys. Res.,* **86**(B4), 2825–2852.

Ekström, G., Nettles, M. & Dziewoński, A., 2012. The global CMT project 2004–2010: centroid-moment tensors for 13,017 earthquakes, *Phys. Earth planet. Inter.,* **200**, 1–9.

Ellis, S. & Stöckhert, B., 2004. Elevated stresses and creep rates beneath the brittle-ductile transition caused by seismic faulting in the upper crust, *J. geophys. Res.,* **109**(B5), doi:10.1029/2003JB002744.

Farr, T.G. *et al.*, 2007. The Shuttle Radar Topography Mission, *Rev. Geophys.,* **45**(2), doi:10.1029/2005RG000183.

Freed, A.M., 2005. Earthquake triggering by static, dynamic and postseismic stress transfer, *Ann. Rev. Earth planet. Sci.,* **33**(1), 335–367.

Freed, A.M. & Lin, J., 1998. Time-dependent changes in failure stress following thrust earthquakes, *J. geophys. Res.,* **103**(10), 24 393–24 409.

Fukushima, Y., Takada, Y. & Hashimoto, M., 2013. Complex ruptures of the 11 April 2011 Mw 6.6 Iwaki earthquake triggered by the 11 march 2011 Mw 9.0 Tohoku earthquake, Japan, *Bull. seism. Soc. Am.,* **103**(2B), 1572–1583.

Fukushima, Y., Toda, S., Miura, S., Ishimura, D., Fukuda, J., Demachi, T. & Tachibana, K., 2018. Extremely early recurrence of intraplate fault rupture following the Tohoku-Oki earthquake, *Nat. Geosci.,* **11**(10), 777–781.

Hainzl, S., 2004. Seismicity patterns of earthquake swarms due to fluid intrusion and stress triggering, *Geophys. J. Int.,* **159**(3), 1090–1096.

Hayes, G.P., 2017. The finite, kinematic rupture properties of great-sized earthquakes since 1990, *Earth planet. Sci. Lett.,* **468**, 94–100.

Hu, Y., Bürgmann, R., Uchida, N., Banerjee, P. & Freymueller, J.T., 2016. Stress-driven relaxation of heterogeneous upper mantle and time-dependent afterslip following the 2011 Tohoku earthquake, *J. geophys. Res.,* **121**(1), 385–411.

Hubbert, M.K. & Rubey, W.W., 1959. Mechanics of fluid-filled porous solids and its application to overthrust faulting, *Bull. Geol. Soc. Am.,* **70**(2), 115–166.

Ikari, M.J., Marone, C., Saffer, D.M. & Kopf, A.J., 2013. Slip weakening as a mechanism for slow earthquakes, *Nat. Geosci.,* **6**(6), 468–472.

Imanishi, K., Ando, R. & Kuwahara, Y., 2012. Unusual shallow normal-faulting earthquake sequence in compressional northeast Japan activated after the 2011 off the Pacific coast of Tohoku earthquake, *Geophys. Res. Lett.,* **39**(9), doi:10.1029/2012GL051491.

Kagan, Y.Y., Jackson, D.D. & Geller, R.J., 2012. Characteristic earthquake model, 1884-2011, R.I.P., *Seismol. Res. Lett.,* **83**(6), doi:10.1785/0220120107.

Kato, A., Sakai, S. & Obara, K., 2011. A normal-faulting seismic sequence triggered by the 2011 off the Pacific coast of Tohoku Earthquake: Wholesale stress regime changes in the upper plate, *Earth, Planets Space,* **63**(7), 745–748.

King, G. C.P., Stein, R.S. & Lin, J., 1994. Static stress changes and the triggering of earthquakes, *Bull. seism. Soc. Am.,* **84**(3), 935–953.

Komura, K., Aiyama, K., Nagata, T., Sato, H.P., Yamada, A. & Aoyagi, Y., 2019. Surface rupture and characteristics of a fault associated with the 2011 and 2016 earthquakes in the southern Abukuma Mountains, northeastern Japan, triggered by the Tohoku-Oki earthquake, *Earth, Planets Space,* **71**(1), 1–23.

McCaffrey, R. & Abers, G., 1988. Syn3: a program for inversion of teleseismic body waveforms on microcomputers, Technical Report, Accession Number: ADA198940, Southeastern Center for Electrical Engineering,St. Cloud, FL, USA.

Murray, J. & Segall, P., 2002. Testing time-predictable earthquake recurrence by direct measurement of strain accumulation and release, *Nature,* **419**(6904), 287–291.

Muto, J., Moore, J.D., Barbot, S., Iinuma, T., Ohta, Y. & Iwamori, H., 2019. Coupled afterslip and transient mantle flow after the 2011 Tohoku earthquake, *Sci. Adv.,* **5**(9), doi:10.1126/sciadv.aaw1164.

Nabalek, J., 1984. Determination of earthquake source parameters from inversion of body waves, *PhD thesis*, Massachusetts Institute of Technology, Cambridge, MA, USA.

Okada, T., Yoshida, K., Ueki, S., Nakajima, J., Uchida, N., Matsuzawa, T., Umino, N. & Hasegawa, A., 2011. Shallow inland earthquakes in NE Japan possibly triggered by the 2011 off the Pacific coast of Tohoku Earthquake, *Earth, Planets Space,* **63**(7), 749–754.

Okada, Y., 1992. Internal deformation due to shear and tensile faults in a half-space, *Bull. seism. Soc. Am.,* **82**(2), 1018–1040.

Ozawa, S., Nishimura, T., Suito, H., Kobayashi, T., Tobita, M. & Imakiire, T., 2011. Coseismic and postseismic slip of the 2011 magnitude-9 Tohoku-Oki earthquake, *Nature,* **475**(7356), 373–376.

Reid, H.F., 1910. The Mechanics of the Earthquake, The California Earthquake of April 18, 1906, Technical report, Carnegie Institution of Washington, Washington, DC.

Roeloffs, E. & Langbein, J., 1994. The earthquake prediction experiment at Parkfield, California, *Rev. Geophys.,* **32**(3), 315–336.

Sato, T., Kazahaya, K., Matsumoto, N. & Takahashi, M., 2020. Deep groundwater discharge after the 2011 Mw 6.6 Iwaki earthquake, Japan, *Earth, Planets Space,* **72**(1), doi:10.1186/s40623-020-01181-7.

Shapiro, S.A., Huenges, E. & Borm, G., 1997. Estimating the crust permeability from fluid-injection-induced seismic emission at the KTB site, *Geophys. J. Int.,* **131**(2), 5–8.

Sieh, K. *et al.*, 2008. Earthquake supercycles inferred from sea-level changes recorded in the corals of west Sumatra, *Science,* **322**(5908), 1674–1678.

Taymaz, T., Jackson, J.A. & Westaway, R., 1990. Earthquake mechanisms in the Hellenic Trench near Crete, *Geophys. J. Int.,* **102**(3), 695–731.

Thatcher, W., Matsuda, T., Kato, T. & Rundle, J.B., 1980. Lithospheric loading by the 1896 Riku-u earthquake, northern Japan: implications for plate flexure and asthenospheric rheology, *J. geophys. Res.,* **85**(B11), 6429–6435.

Toda, S., Stein, R.S., Sevilgen, V. & Lin, J., 2011. Coulomb 3.3 Graphic-rich deformation and stress-change software for earthquake, tectonic, and volcano research and teaching-user guide, U.S. Geological Survey Open-File Report 2011–1060, 63pp., available at https://pubs.usgs.gov/of/2011/1060/.

Toda, S. & Tsutsumi, H., 2013. Simultaneous reactivation of two, sub-parallel, inland normal faults during the Mw 6.6 11 April 2011 Iwaki earthquake triggered by the Mw 9.0 Tohoku-oki, Japan, earthquake, *Bull. seism. Soc. Am.,* **103**(2B), 1584–1602.

Twardzik, C., Vergnolle, M., Sladen, A. & Avallone, A., 2019. Unravelling the contribution of early postseismic deformation using sub-daily GNSS positioning, *Sci. Rep.,* **9**(1), 1775, doi:10.1038/s41598-019-39038-z.

Uchide, T. & Imanishi, K., 2018. Underestimation of microearthquake size by the magnitude scale of the Japan Meteorological Agency: influence on earthquake statistics, *J. geophys. Res.,* **123**(1), 606–620.

Virtanen, P. *et al.*, 2020. SciPy 1.0: fundamental algorithms for scientific computing in Python, *Nat. Methods,* **17**(3), 261–272.

Waldhauser, F. & Ellsworth, W.L., 2000. A double-difference earthquake location algorithm: method and application to the Northern Hayward Fault, California, *Bull. seism. Soc. Am.,* **90**(6), 1353–1368.

Walters, R.J. *et al.*, 2018. Dual control of fault intersections on stop-start rupture in the 2016 Central Italy seismic sequence, *Earth planet. Sci. Lett.,* **500**, 1–14.

Wang, K., Zhu, Y., Nissen, E. & Shen, Z.K., 2021. On the relevance of geodetic deformation rates to earthquake potential, *Geophys. Res. Lett.,* **48**(11), e2021GL093231, doi:10.1029/2021GL093231.

Wang, S., Xu, W., Xu, C., Yin, Z., Bürgmann, R., Liu, L. & Jiang, G., 2019. Changes in groundwater level possibly encourage shallow earthquakes in central Australia: the 2016 Petermann Ranges earthquake, *Geophys. Res. Lett.,* **46**(6), 3189–3198.

Wdowinski, S., Bock, Y., Zhang, J., Fang, P. & Genrich, J., 1997. Southern California Permanent GPS Geodetic Array: spatial filtering of daily positions for estimating coseismic and postseismic displacements induced by the 1992 Landers earthquake, *J. geophys. Res.,* **102**(B8), 18 057–18 070.

Yoshida, K., Hasegawa, A. & Okada, T., 2015. Spatially heterogeneous stress field in the source area of the 2011 Mw 6.6 Fukushima-Hamadori earthquake, NE Japan, probably caused by static stress change, *Geophys. J. Int.,* **201**(2), 1062–1071.

Yoshida, K., Saito, T., Urata, Y., Asano, Y. & Hasegawa, A., 2017. Temporal changes in stress drop, frictional strength, and earthquake size distribution in the 2011 Yamagata-Fukushima, NE Japan, Earthquake Swarm, caused by fluid migration, *J. geophys. Res.,* **122**(12), 10 379–10 397.

Yoshida, K., Uchida, N., Hiarahara, S., Nakayama, T., Matsuzawa, T., Okada, T., Matsumoto, Y. & Hasegawa, A., 2020. 2019 M6.7 Yamagata-Oki earthquake in the stress shadow of 2011 Tohoku-Oki earthquake: was it

caused by the reduction in fault strength?, *Tectonophysics,* **793**, doi:10.1016/j.tecto.2020.228609.

Zakharova, O., Hainzl, S. & Bach, C., 2013. Seismic moment ratio of aftershocks with respect to main shocks, *J. geophys. Res.,* **118**(11), 5856–5864.

Zebker, H.A. & Lu, Y., 1998. Phase unwrapping algorithms for radar interferometry: residue-cut, least-squares, and synthesis algorithms, *J. Opt. Soc. Am., A,* **15**(3), 586–598.

Zwick, P., McCaffrey, R. & Abers, G., 1994. MT5 Program, *IASPEI Software Library*, 4.

SUPPORTING INFORMATION

Supplementary data are available at *GJI* online.

Figure S1. Coseismic LOS displacements and microseismicity, highlighting the position of a conjugate fault in the hangingwall of the Mochiyama Fault. (a) Coseismic displacements in the 2011 Mochiyama earthquake measured by ALOS-1 between 20110220 and 20110320. (b) Spatial distribution of microseismicity from the catalogue of Uchide and Imanishi [2018]. The focal mechanisms shown in (a) and (b) are from the F-NET catalogue and are foreshocks that occurred between the 11th March 2011 Tohoku-oki and 19th March 2011 Mochiyama earthquakes. (c) Profile through the coseismic LOS displacements from the Profile shown in (a). (d) Cross-sectional Profile through the relocated microseismicity. Each event is scaled by the moment magnitude, and the time of each event relative to the 11th March 2011 Tohoku-oki earthquake are shown by the colour. The microseismicity data highlight the main shock fault plane as being planar and extending down to 10 km depth. Within the fault hangingwall, there is a second concentration of seismicity that appears to delineate a conjugate fault dipping towards the northeast (right in the figure). The location of this fault correlates with the hypocentral locations of M_w 4 and five earthquakes that occurred between the 11th March and 18th March 2011 in the NEID catalogue (see Fig. 4 in the main text).

Figure S2. Forward models of the coseismic strain field predicted by the original slip model of Fukushima *et al*. (2018) with moment rescaled to 10×10^{17} Nm (left-hand panel) and for a model with moment rescaled to 6×10^{17} Nm (right-hand panel). Inset is the misfit between the observed and predicted across-fault strain within the two triangles that span the fault as a function of the moment release. The vertical grey bar shows the range of moment release for the 2011 Mochiyama earthquake derived from the body-waveform modelling discussed in Section 2.1. Misfit is calculated as: $\sum[(\epsilon_{min}^{obs} - \epsilon_{min}^{mod})^2]^{1/2}$, where ϵ_{min}^{obs} is the observed minimum principal strain and ϵ_{min}^{mod} is the modelled minimum principal strain. These calculations demonstrate that the slip model of Fukushima *et al*. (2018) significantly overpredicts the observed across-fault strain caused by the 2011 Mochiyama earthquake. We found that varying the slip distribution has little effect on the misfit between the models and the GPS data.

Figure S3. Incremental strain for the pre-Tohoku-oki period between 2005 and 2011 (a), Tohoku-oki coseismic strain (b), the early (7-d) Tohoku-oki post-seismic strain prior to the 19th March Mochiyama earthquake (c), and 1-yr of post-seismic after the 2016 Mochiyama earthquake (d). Note that in (c) a number of the coastal GPS stations were damaged by the tsunami, limiting our ability to determine the strain around the Mochiyama Fault over this time period.

Figure S4. Time-series of the baseline length change between GPS stations 960581 and 950214 that span the Mochiyama Fault following the 2011 earthquake (red) and the 2016 earthquake (blue). The locations of these stations are shown on Fig. 5 in the main text. On

the left we show the raw baseline length change time-series, demonstrating the logarithmic temporal evolution of across-fault stretching after both events. The time-series after the 2011 Mochiyama earthquake contains a static offset related to the April 2011 Iwaki earthquake sequence. On the right we show the trajectory model fits to these time-series after removing the step related to coseismic displacements in the Iwaki earthquake, normalized by the amplitude after 1 yr. The two models have almost identical relaxation times, suggesting that the mechanisms driving across-fault extension did not experience a significant change in the property that controls the decay time of earthquake stress changes. However, there is a factor 10 difference in the amplitude of the across-fault strain.

Figure S5. Slip distribution in the two Mochiyama earthquakes compared with the pattern of microseismicity. Panels (a) and (b) show the slip distributions derived by Fukushima *et al.* (2018) compared with the earthquake hypocentral locations of earthquakes within 5 km of the fault from the catalogue of Uchide & Imanishi (2018). Note the sharp cut-off at 10 km depth and the way the seismicity mostly wraps around the coseismic rupture area. (c) and (d) shows the spatially binned moment release within the two aftershock sequences. Summing the moment release in (c) over the patches that contain moment release $>1 \times 10^{12}$ Nm yields ∼20 cm of seismic slip in the region directly beneath the coseismic rupture area and <10 km depth.

Figure S6. Plots showing the shear stress recovery $\Delta \tau_p = \Delta \tau_c$ against the depth on the rupture normalized by the thickness of the elastic layer z_e, as in Fig. 7 of the main text. The left-hand plot shows the effect of varying the along-strike area that is able to slide through afterslip in response to coseismic stress changes L_f. We performed calculations with L_f equal to 2, 3, 4, 5, 7.5, 10 and 12 km in models that rupture all the way to the base of the elastic layer and which include mechanically-coupled afterslip and viscoelastic relaxation. Changing L_f clearly has a relatively small effect (∼5 per cent) on the amplitude of the shear stress recovery, with larger L_f causing larger shear stress recovery. Once L_f is greater than 5 km, changing its value makes little difference to the shear stress recovery. The right-hand plot shows the effect of changing the elastic moduli of the seismogenic layer on the estimate of shear stress recovery for a 20, 30 and 40 GPa shear modulus. All results plot on top of one another, indicating that changing the elastic moduli make no difference to the estimated shear stress recovery. This feature of the models reflects the fact that, for a constant slip, changing the elastic moduli will cause a proportional change in the stress changes in the surrounding medium, which cause a proportional change in the amount of post-seismic deformation and reloading.

Figure S7. Fault clamping ($\Delta \sigma_p = \Delta \tau_c$) results for the generalized models in the same format as Fig. 7 in the main text. By convention, positive values represent increases in fault normal stress that clamp the fault. These models show that stress changes on the main shock caused by viscoelastic relaxation dominate the fault clamping by bending the overlying elastic layer. There is a change in the sign of the fault clamping within the middle of the layer at $z/z_e = 0.5$ (see a–c). Afterslip does not lead to significant changes in fault clamping, because the majority of the deformation is contained within the plane of the fault (d–f). Small deviations in fault clamping within the shallow part of the elastic layer in the models (c–f) may reflect numerical artefacts associated with the modelling, and therefore we do not interpret them here. The mechanically coupled models (g–i) show that fault clamping is always <0.2. When scaled by the effective friction (0.01–0.4), changes in fault clamping will

therefore only contribute to <0.2−8 per cent of the change in failure stress.

Figure S8. Fault clamping ($\Delta \sigma_p = \Delta \tau_c$) for the models shown in Fig. 8 in the main text in which only the stress changes caused by the 2011 Mochiyama earthquake are relaxed by post-seismic deformation. These calculations demonstrate that almost everywhere the fault clamping is ≪10 per cent, and therefore makes a minor contribution to changes in the fault failure stress. This result is expected, because the fault ruptured only 80 per cent of the seismogenic crust and therefore caused limited viscoelastic relaxation. Fig. S7 showed that post-seismic deformation through viscoelastic relaxation dominates any fault clamping effects, but when the fault only ruptures part of the elastic layer the fault clamping is negligible.

Figure S9. Coseismic slip distribution (left-hand panel) and stress drop (right-hand panel) in the 2011 Mochiyama earthquake using the slip distribution of Fukushima *et al.* (2018) when all areas with slip less than some critical value (0.1, 0.2 and 0.3 m) are removed and the moment is rescaled across the remainder of the rupture area. This process results in a compaction of the coseismic slip distribution, and an in increase in the average stress drop on the rupture area.

Figure S10. Modelled coseismic (left-hand panel) and post-seismic (right-hand panel) deformation due to slip in the April 2011 Iwaki earthquake sequence based on the fault geometries and slip distributions of Fukushima *et al.* (2013). We simplify the models by using the fault-averaged slip from the slip distributions of Fukushima *et al.* (2013), which has little effect on the predicted amplitude of deformation or stress changes at tens of kilometres from the Iwaki faults.

Figure S11. Co- and post-seismic stress changes due to the Iwaki earthquake sequence resolved on the Mochiyama Fault. These models do not include distributed viscoelastic relaxation beneath the Iwaki and Mochiyama Faults, but are otherwise identical to those shown in Fig. 10 of the main text.

Figure S12. Post-seismic stress changes due to the relaxation of coseismic stress changes in the Tohoku-oki earthquake resolved onto the Mochiyama Fault calculated from the numerical model of Hu *et al.* (2016).

Figure S13. Comparison between the stress-driven models of post-seismic deformation and the kinematic afterslip model discussed in Section 3.2.4 of the main manuscript. The surface deformation for the stress-driven model that includes viscoelastic relaxation and afterslip is shown in (a), and the best-fitting kinematic afterslip with 80 cm of shallow afterslip and 20 cm of deep afterslip is shown in (b). The corresponding afterslip distributions are shown in (c) and (d). Otherwise, the format of the figure is the same as that of Fig. 8 in the main manuscript.

Figure S14. Spatio-temporal evolution of the aftershocks following the 2011 and 2016 earthquakes on the Mochiyama Fault from the region shown in Fig. 5 in the main text. The reference point was the centre of the Mochiyama Fault at the surface. Aftershocks are shown by small black dots, whilst light red dots represent aftershocks of M_j > 4 scaled by earthquake magnitude. (a) Full seismicity time-series from 2010 to 2019. The dark grey line marks the moving average of earthquake locations and the dashed lines are ±1 standard deviation. (b) Zoom of the seismicity around the 2011 Mochiyama earthquake. The horizontal blue bars mark the time-extent of the primary and secondary images used to form interferograms in Fukushima *et al.* (2018). The vertical red-dashed line marks the time of the 2011 Mochiyama earthquake. (c) Zoom of the seismicity around the 2016 Mochiyama earthquake. The 2011 event was clearly predated by a number of foreshocks in close proximity to the main

shock and was followed by a swarm of seismicity with no clear main shock–aftershock sequences. We cannot see any clear migration of seismicity from depth towards the surface in the earthquake location time-series.

Table S1. Earthquake source parameters for the 2011 and 2016 earthquakes on the Mochiyama Fault. InSAR-derived source parameters are from Fukushima *et al*. (2018). All moment estimates have been calculated using a shear modulus of 30 GPa. z is the centroid depth, s is the strike, d is the dip and r is the rake. STF is the source–time function length and %DC is the percentage double-couple of the moment tensor.

Please note: Oxford University Press is not responsible for the content or functionality of any supporting materials supplied by the authors. Any queries (other than missing material) should be directed to the corresponding author for the paper.